Deviations from the Local Hubble Flow. I. The Tip of the Red Giant Branch as a Distance Indicator

Bryan Méndez[1], Marc Davis[1,2], John Moustakas[3], Jeffrey Newman[1], Barry F. Madore[4], and Wendy L. Freedman[4]

ABSTRACT

The properties of the velocity field in the local volume ($cz < 550$ km s^{-1}) have been difficult to constrain due to a lack of a consistent set of galaxy distances. The sparse observations available to date suggest a remarkably quiet flow, with little deviation from a pure Hubble law. However, velocity field models based on the distribution of galaxies in the 1.2 Jy IRAS redshift survey, predict a quadrupolar flow pattern locally with strong infall at the poles of the local Supergalactic plane. We probe this velocity field and begin to establish a consistent set of galactic distances. We have obtained images of nearby galaxies in the I and V band from the W.M. Keck Observatory and in F814W and F555W filters from the *Hubble Space Telescope*. Where these galaxies are well resolved into stars we can use the Tip of the Red Giant Branch (TRGB) as a distance indicator. Using a maximum likelihood analysis to quantitatively measure the I magnitude of the TRGB we determine precise distances to seven nearby galaxies: Leo I, Sextans B, NGC 1313, NGC 3109, UGC 03755, UGC 06456, and UGC 07577.

Subject headings: stars: luminosity function – stars: Population II – galaxies: distances – cosmology: observations – large-scale structure of universe

1. Introduction

1.1. Local Deviations from Hubble Flow

Although tremendous progress has been made in recent years in mapping the large-scale gravitational field (out to scales of $cz \sim 10,000$ km s^{-1}), relatively little data are available to study the velocity field of galaxies in the local neighborhood (≤ 500 km s^{-1}). The major impediment to constraining the local flow is the lack of a consistent set of distances to nearby galaxies. Locally,

[1]Department of Astronomy, 601 Campbell Hall, University of California, Berkeley, CA 94720-3411.

[2]Department of Physics, 366 LeConte Hall, University of California, Berkeley, CA 94720-7300.

[3]Steward Observatory, 933 North Cherry Avenue, University of Arizona, Tucson, AZ 85721

[4]Observatories of the Carnegie Institute of Washington, 813 Santa Barbara St., Pasadena, CA 91101.

the deviations from a pure Hubble law have been predicted to be large and measurable, as much as 1 magnitude in distance modulus.

If gravitational instability has generated all the large scale structure in the Universe, then it must also be responsible for the extremely anisotropic local galaxy distribution (see Fig. 1) (Peebles 1993). Under this assumption, it is possible to predict the velocity field from this distribution. The catalogs from such full–sky galaxy redshift surveys as the 1.2 Jy IRAS survey (Fisher et al. 1994) allow us to estimate the large scale gravity field out to a redshift $cz \approx 8,000$ km s^{-1}. In the limit of linear perturbations at late times, one expects the peculiar velocity at a point in space to be proportional to the gravity field at that point. Fig. 1 demonstrates that according to linear theory, the local velocity field is expected to show substantial deviations from uniformity, with quadrupole distortions dominating. Outflow is directed toward Virgo and Fornax on opposite sides of the sky, while substantial infall occurs from the poles of the local distribution. Such a flow is expected within any gravitational model and would act to depopulate galaxies from the local poles. The bulk of the local galaxy distribution does reside on the positive and zero contours of Figure 1 (the local supercluster plane), while the regions of negative peculiar velocity are deficient but not entirely devoid of galaxies. It is possible that linear theory does not apply on this scale, but in that case one would expect a more chaotic flow of similar amplitude.

Observations of local deviations from Hubble flow do not really support the expectations of Fig. 1, especially in the southern direction (see the review by Burstein (1990)). However, the data are sparse because large spiral galaxies suitable for Tully-Fisher or Cepheid Period–Luminosity analysis are very rare locally, and the sky coverage, particularly in the expected infalling regions, is poor. We have thus set out to provide new distances to a complementary sample of nearby galaxies that were chosen to lie near the maximum predicted infall.

1.2.   A Consistent Distance Scale for Nearby Galaxies: The Tip of the Red Giant Branch (TRGB)

According to stellar evolution theory, the tip of the first–ascent red–giant branch (TRGB) marks the onset of the core–helium flash in low–mass stars. Observationally, this phenomenon causes a distinct and abrupt termination of the bright end of the red–giant branch luminosity function. This discontinuity translates directly into an excellent distance indicator: the bolometric luminosity of the TRGB for low–mass stars is predicted to vary by only ~ 0.1 mag for ages ranging from 2 up to 15 Gyr (Iben & Renzini 1983) and for metallicities encompassing the entire range represented by Galactic globular clusters ($-2.1 < [Fe/H] < -0.7$) (Salaris & Cassisi 1997). The discontinuity is also found empirically to be stable at the ~ 0.1 mag level in the I band for the same set of stellar properties.

The TRGB method has a strong empirical, as well as physical, basis. Distances obtained using the TRGB agree with the Cepheid Period–Luminosity relation (where direct comparisons have

been made) at a $\pm 5\%$ level, e.g. Lee et al. (1993); Sakai et al. (1996); Udalski et al. (2001) – an exception is for M33: Kim et al. (2002). Furthermore, since all visible galaxies must have had a first generation of stars, the TRGB method is applicable to populations in all morphological types, including spiral, elliptical, and even irregular galaxies, provided their metallicity is sufficiently low. The TRGB method also requires far less telescope time for observations than Cepheids since repeat visits are unnecessary, a considerable advantage. A good review of the TRGB, its applications and theoretical underpinnings, is given in Madore & Freedman (1998).

We have used the Tip of the Red Giant Branch to obtain distances to a sample of local galaxies (mostly dwarfs) in order to derive their peculiar velocities. In § 2 we discuss the observations we have made of several galaxies using both the W.M. Keck observatory and the *Hubble Space Telescope* (*HST*). In § 3 we present the methods for measuring the TRGB that we have employed and include detailed information on the analysis and error propogation. Finally, in § 4 we present the Color–Magnitude Diagrams, Luminosity Functions, and derived distances for several of the galaxies studied. We discuss the derived peculiar velocities and their implications in paper II (Méndez et al. 2002).

2. Data

To select targets for observation, we assembled an all-sky sample of 502 galaxies likely to be in the local volume (cz $\lesssim$550 km s^{-1}) . This sample consists of all objects identified as galaxies (Type G) with heliocentric radial velocities less than +900 km s^{-1} within the NASA/IPAC Extragalactic Database (NED)[5]. We then transformed all velocities to the Local Group frame (Karachentsev & Makarov 1996) and selected those having radial velocities less than +550 km s^{-1}. Their distribution on the sky (in Galactic coordinates) is shown in Fig. 1. Undoubtedly, many (~ 100) of these galaxies are not actually within the local neighborhood but are cluster members whose large peculiar velocities arising from virial motions bring them into our sample. This is clearly the case toward the Virgo cluster ($l = 283.78°$, $b = 74.49°$). We are most interested in galaxies located in the regions of strong infall predicted by the flow models of Nusser & Davis (1994) and Baker et al. (1998). We have observed a subset of these galaxies with the Keck Telescope in Hawaii and/or the *Hubble Space Telescope.*

2.1. Keck Observations and Reduction

We observed target galaxies on the nights of 1997 December 22 and 23 under photometric conditions using the Low Resolution Imaging Spectrometer (LRIS) (Oke et al. 1995). At that time

---

[5]The NASA/IPAC Extragalactic Database (NED) is operated by the Jet Propulsion Laboratory, California Institute of Technology, under contract with the National Aeronautics and Space Administration.

LRIS operated at the Cassegrain focus of the 10-m Keck II telescope at the W.M. Keck Obseratory located on Mauna Kea, Hawaii (it now resides on Keck I). The instrument includes a backside-illuminated Tek 2048×2048 CCD detetector with an imaging scale of 0.215 arcseconds/pixel and a field of view of 6×8 arcminutes. We read out the CCD in the two-amplifier mode.

Each galaxy was observed through both Johnson V and Cousins I broadband filters. For the brightest, best resolved galaxies we took one exposure in each filter, of typically 300 sec duration . For the fainter, less well–resolved galaxies we took between three and eight 250–500 second exposures in I and one to two 300–800 second exposures in V. See Table 1 for details. Over both nights four Landolt standard star fields were observed (Landolt 1992) in order to calibrate the photometry.

The images were reduced according to standard procedures using software written in IDL. The CCD frames were subtracted for bias level (determined from the overscan region appropriate to that amplifier) and dark current. The right side of each frame was scaled to match the left using the gain (1.97 e^-/count for the left amplifier, 2.1 e^-/count for the right) and the respective bias levels. In I sky flats were constructed using all of a single night's image frames themselves, while in V dome flats were used to remove pixel-to-pixel variations. The resulting image frames were found to be uniform in sensitivity across their widths to better than 1% . Frames for individual galaxies were registered and combined through a median filter to remove cosmic rays and increase the signal-to-noise ratio. These combined frames were used for finding stars.

Due to geometric and optical distortions, the point spread function (PSF) varies as a function of position on the LRIS CCD chip. It was therefore necessary to compute an empirical PSF for each image from a hand-selected list of $10 - 30$ bright, unsaturated stars that had no stellar neighbors within $\sim 3 \times$FWHM. The PSF for each data image was modeled using the DAOPHOT package within IRAF[6]. Stars were identified and instrumental magnitudes were computed using the FORTRAN versions of DAOPHOT II/ALLFRAME (Stetson 1987, 1994). These programs, modified for FITS I/O, were obtained from K. Gebhardt at the University of California, Santa Cruz. Several of the fainter targets were not well resolved into stars, and thus were not usable for determining TRGB distances. Thus, we did not perform full photometry on these objects.

The instrumental magnitudes m_{inst} and magnitude errors for each image in a filter were combined using a robust mean (a weighted mean iteratively refined by a factor of $1/(1 + \chi_i^2)$ for each weight, w_i) and converted to standard magnitudes m_{stand} with the equation

$$m_{\mathrm{stand}} = m_{\mathrm{inst}} + 2.5\log(t) + \mathrm{ac} - \mathrm{c}_1 - \mathrm{c}_2 X - \mathrm{c}_3(V - I) - \mathrm{c}_4 X(V - I) \qquad (1)$$

where t is the exposure time, ac is the aperture correction, X is the airmass for each observation, and c_1, c_2, c_3, and c_4 are constants. The aperture correction, ac, was computed by comparing the

---

[6]IRAF is distributed by the National Optical Astronomy Observatories, which is operated by the Association of Universities for Research in Astronomy, Inc., under contract to the National Science Foundation.

magnitudes of bright isolated stars in each object found through an aperture of 40 pixels (8.6 arcsec) in diameter to the magnitude found via PSF fitting. Values of the aperture corrections range from 0.00 to -0.10 mag, with standard errors of 0.01 to 0.03 mag. The broadband filters on LRIS are very close to the standard system, so the color terms, c_3 and c_4, were found to be negligable. The extinction coefficients (in magnitudes/airmass) given by c_2 are 0.12 at 550 nm and 0.07 at 800 nm (Beland et al. 1988). The magnitude zero point, c_1, was computed by using the above information and aperture photometry of both Landolt standard stars and the additional stars in Landolt fields recently calibrated to the standard system (Stetson 2000). The interactive IRAF task *fitparams* in the **noao.digiphot.photcal** package was used to compute a non-linear least squares fit of the observed magnitudes to the calibrated magnitudes of these standards. The resulting zero points have an rms error of 0.02 mag in both I and V.

2.2. *HST* Observations and Reduction

We also obtained images of thirteen galaxies with the Wide Field Planetary Camera 2 (WFPC2) aboard the *Hubble Space Telescope*[7] between August 13, 1999 and May 9, 2000 (program 8199, PI M. Davis). Galaxies were observed in two exposures from 1200 - 1300s each in the F814W filter; three objects were also observed with two 1200 - 1300s exposures in the F555W filter. Table 1 details the WFPC2 observations. These thirteen galaxies were chosen specifically because they are located in regions of the sky where strong inflow is predicted by the IRAS data, especially around $l = 170° - 240°$ and $b = 10° - 30°$.

The calibrated and data–quality images were retrieved from the Space Telescope Science Institute (STScI) where preliminary CCD processing, including bias- and dark-subtraction, flat–fielding, and a shutter–shading correction, are automatically applied using calibration data closest to the time of the observation. Details of these initial reductions are given in Burrows (1994) and Holtzman et al. (1995).

For photometric measurements we used the PSF-fitting package HSTphot[8] developed by A. Dolphin specifically for analyzing HST/WFPC2 data. HSTphot has been used recently in a number of stellar population studies (Wyder 2001; Saha et al. 2001; Dolphin et al. 2001; Seitzer et al. 2001). It has been optimized for the undersampled conditions present in WFPC2 data and works very well in crowded fields. HSTphot is written in C and runs non-interactively from the command line. In our reductions, HSTphot was an order of magnitude faster than ALLFRAME, and identified $10-30\%$ more stars. The algorithms used by HSTphot most resemble those of DoPHOT (Schechter

---

[7]Observations made with the NASA/ESA *Hubble Space Telescope*, obtained at the Space Telescope Science Institute, which is operated by the Association of Universities for Research in Astronomy, Inc., under NASA contract NAS 5-26555. These observations are associated with proposal # 8199.

[8]The source code and documentation for HSTphot can be obtained at http://www.noao.edu/staff/dolphin/hstphot.

et al. 1993); tests of HSTphot photometry including a comparison with an independent DoPHOT analysis are discussed in Dolphin (2000b). Our own limited tests of HSTphot reliability as measured against ALLFRAME photometry showed no gross systematics, even at faint magnitudes.

HSTphot determines stellar magnitudes using a library of Tiny Tim PSFs (Krist & Hook 1996) that have been built for all the commonly used WFPC2 filters. The PSFs are modified internally for geometric distortions using the equations of Holtzman et al. (1995), and corrected for the 34th row error (Shaklan et al. 1995). The final stellar magnitudes are calibrated using the charge-transfer efficiency and zero-point corrections derived in Dolphin (2000a).

The data were analyzed using HSTphot according to the following recipe: (1) mask bad pixels and columns using the data-quality image; (2) reject cosmic rays; (3) flag and mask hot pixels; (4) generate a sky image; (5) find stars and make photometric measurements; and (6) determine and apply aperture corrections. The output from the *multiphot* procedure in HSTphot was trimmed according to the following criteria to generate the final, calibrated star list: $\chi^2 < 5$, $-0.5 <$ sharpness < 0.5, S/N > 3.5, and class < 3.

We augmented our sample of HST data by searching the WFPC2 archive[9] for suitable nearby galaxies with observations in the F814W and F555W filters. The blue compact dwarf galaxy UGC 06456 was found to have a well defined TRGB as discussed in more detail in § 4.3.6. These data were reduced in the same way as described above.

3. Measuring the TRGB

3.1. Detection of the TRGB

Early estimates of the apparent magnitude of the TRGB used a simple "eyeball" estimate of its location in a Color-Magnitude Diagram (CMD), e.g. Mould & Kristian (1986). In the 1990s more quantitative methodologies were introduced (Lee et al. 1993). In our analysis we have used two distinct methods to quantitatively estimate the TRGB magnitude from the shape of the luminosity function of a population of stars.

After the exhaustion of hydrogen fuel in the core of a star there is a rapid increase in the rate at which its luminosity will change with time. Because this evolution is so quick, stars that appear above the main sequence turnoff point in the CMD must have had the same Main Sequence lifetime, and hence the same initial mass, to within a few percent. Therefore, the luminosity function of a star cluster (or single population of stars) past the Main Sequence is primarily a reflection of the rate of luminosity evolution for those stars. See the review by Renzini & Fusi Pecci (1988) for

---

[9]Data are based on observations made with the NASA/ESA *Hubble Space Telescope*, obtained from the Data Archive at the Space Telescope Science Institute, which is operated by the Association of Universities for Research in Astronomy, Inc., under NASA contract NAS 5-26555. These observations are associated with proposal # 6276.

details in interpreting the luminosity functions of populations of evolved stars.

Low-mass, post-main-sequence stars develop an inert isothermal core supported by electron degeneracy pressure. The luminosity of these stars is almost entirely dependent on the mass of that core, because all of their energy generation occurs in a thin hydrogen burning shell surrounding the core. The temperature of the shell is set by the amount of potential energy converted to heat by the gravitational contraction of the core. Once on the red giant branch (the vertical track in the CMD) the stars' rate of luminosity evolution is primarily dependent on the rate of increase of the mass of the core.

Due to the simple dependence of luminosity on core mass, red giant branch luminosity functions are expected to be very simple and depend only very weakly on parameters such as age, metallicity, or mass of the envelope of the star. Indeed theoretical and empirical studies find the bright end of red giant branch luminosity functions to have a simple power-law behavior; i.e., they are straight lines in the magnitude-log(counts) plane (Zoccali & Piotto 2000). Models all predict essentially the same power-law slope and are in excellent agreement with observations.

The luminosity function of the red giant branch terminates at the TRGB, the core mass at which the helium flash occurs, and the stars then adjust their structures rapidly and move to a new location in the CMD (the Horizontal Branch of helium core–burning stars). The magnitude of the TRGB is the location in the luminosity function where the red giant branch power–law truncates. Brightward of that break are other populations of stars (asymptotic giant branch and red supergiant stars mostly) but they are rare and have a distinctly different luminosity function behavior.

From our data we have determined that if the red giant branch luminosity function power-law is given as

$$N(m)dm \propto 10^{am}, \tag{2}$$

where m is the apparent magnitude, then $a = 0.30 \pm 0.04$. This fixed slope can also be found in numerous other studies of red giant branch luminosity functions (Zoccali & Piotto 2000, for example) though that fact is rarely explicitly stated.

3.1.1. Discontinuity Detection

The first TRGB estimation method we have applied simply uses the fact that there will be a discontinuity in the luminosity function at the location of the TRGB. The first derivative of the luminosity function should therefore show a large peak at the discontinuity. Early applications often used histograms to approximate the luminosity function and a Sobel edge–detection filter to estimate the first derivative (Lee et al. 1993), but this had the major drawback that the estimates could be strongly dependent on the histogram binning size. Later Sakai et al. (1996, hereafter referred to as SMF96) updated this method by employing a Gaussian-smoothed luminosity function,

$\Phi(m)$, and a continuous edge–detection function

$$E(m) = \Phi(m + \bar{\sigma}_m) - \Phi(m - \bar{\sigma}_m), \tag{3}$$

where $\bar{\sigma}_m$ (as defined by SMF96) is the mean photometric error within a bin of ± 0.05 mag about magnitude m.

We have used the method of SMF96, with some minor modifications, to estimate the TRGB magnitude of our objects. Due to the natural power–law form of the luminosity function we are most concerned with fractional changes. Thus, we use a logarithmic edge–detection function,

$$E(m) = \log_{10}(\Phi(m + \bar{\sigma}_m)) - \log_{10}(\Phi(m - \bar{\sigma}_m)). \tag{4}$$

Another modification to the SMF96 method is the definition of $\bar{\sigma}_m$ used. For each galaxy observed we determine a polynomial fit to our data for the photometric flux errors as a function of flux. The function is then transformed to magnitude error as a function of magnitude. Thus, we define $\bar{\sigma}_m$ as simply the photometric error given by the fit at magnitude m. The region of the luminosity function brighter than the TRGB is sparsely populated (mostly by AGB stars) and thus very noisy; the large first derivative noise spikes can make it difficult to robustly identify the TRGB automatically. We thus weight the edge–detection response by the Poisson noise in the smoothed luminosity function. Even that fails to quiet some noise spikes and we are thus forced to limit this analysis to the region of the luminosity function that we know by inspection contains the TRGB. See the figures in § 4.3 for results of the edge–detection (e.g. Fig. 4)

3.1.2. Maximum Likelihood Analysis

Binning the data is not necessary, and we have employed a maximum likelihood analysis similar in spirit to the luminosity function analysis of Sandage et al. (1979, see also references therein). Define the luminosity distribution function of stars in the galaxy under investigation to be $\phi(m|\mathbf{a})$ where m is the apparent magnitude and $\mathbf{a}$ is the list of parameters defining the function. The probability P that star i has an observed magnitude m_i within a range dm is then

$$P_i = \frac{\phi(m_i|\mathbf{a})dm}{\int_{m1}^{m2} \phi(m|\mathbf{a})dm} \tag{5}$$

where $m1$ and $m2$ are lower and upper bounds for the validity of the parameterized distribution function.

The likelihood $\mathcal{L}$ that the observed distribution of stellar magnitudes is described by this function is simply the product of the individual probablities, since each star is drawn randomly from this distribution. It is most convenient to consider $\ln \mathcal{L}$

$$\ln \mathcal{L} = \sum_i \ln P_i = \sum_i \ln \phi(m_i|\mathbf{a}) - N \ln \left(\int \phi(m)dm \right), \tag{6}$$

where the sum extends over all stars i with N stars in total.

For this analysis we use a simple, broken power-law model to describe the luminosity distribution function, but we also take into account the smoothing induced by measurement errors for the apparent luminosities. We use the form

$$\phi(m) = \int g(m')e(m - m')dm' \tag{7}$$

and define $g(m)$ as

$$g(m) = \begin{cases} 10^{a(m-m_{\mathrm{TRGB}})} & m - m_{\mathrm{TRGB}} > 0 \\ 10^{b(m-m_{\mathrm{TRGB}})-c} & m - m_{\mathrm{TRGB}} < 0 \end{cases} \tag{8}$$

We fix $a = 0.3$ but allow as free parameters the TRGB magnitude m_{TRGB}, the slope of the luminosity function brighter than the TRGB b, and the strength of the discontinuity at the TRGB, c. The smoothing function $e(x)$ is the same error function mentioned in § 3.1.1 used to estimate $\bar{\sigma}_m$. It is a function of the apparent magnitude but not of the parameters of the fit.

Our procedure is then to compute the likelihood function on a grid in the parameters m_{TRGB}, b, and c and to determine the point of maximum likelihood. The method used is self–normalizing; the likelihood contours are quite peaked, with 3σ error widths in m_{TRGB} usually less than 0.1 mag (e.g. Fig 9). To test for covariance we marginalize the likelihood by computing

$$\mathcal{L}(m) = \int_{0.0}^{1.2} \int_{0.5}^{1.0} \mathcal{L}(m, b, c) db\, dc. \tag{9}$$

Covariance with the variables, b, and c is found to be negligible, and the peaks in most of the marginalized likelihoods occur at the same magnitude as the peaks in the full likelihoods. In the cases reported in § 4.3 there are no differences, and the largest difference in all cases is only 0.06 mag. We fit gaussians to the marginalized likelihoods and find that the 1σ errors in m_{TRGB} are typically only a few hundredths of a magnitude.

The best fitting $\phi(m)$ curves for each galaxy are displayed in the figures of § 4.3. Note that these fits are quite acceptable in each case. Smoothing by the photometric errors converts the discontinuity in $g(m)$ at $m = m_{\mathrm{TRGB}}$ into a continuous distribution $\phi(m)$. Since the smoothing becomes larger for fainter magnitudes, the model automatically degrades the apparent slope of the TRGB edge as a function of distance.

The likelihood analysis works best if the red giant branch power–law is observed over a range of one magnitude or more. In cases in which we failed to detect the TRGB, we seldom observed a power law slope for the red giant branch, with crowding and incompleteness effects leading to a rolloff of detected stars that did not fit the TRGB form. In these cases our model for $g(m)$ is inadequate and the likelihood analysis is meaningless. In any event, it is necessary to set the limits of the magnitude range for which the likelihood analysis is performed; it is critical to ensure

that the faint limit avoids regions where incompleteness is non-negligible. The bright limit is less critical, but it obviously must be set brighter than the TRGB. We find that setting it at 0.5 or more magnitudes brighter than the TRGB gives good results.

3.2. Uncertainty in measuring the TRGB

We have used a different approach for estimating random error in the TRGB magnitude from most previous authors. Errors from the method of SMF96 are generally obtained from the Sobel edge–detection response. The uncertainty of I_{TRGB} is taken as either the σ in a Gaussian fit to the peak response or the FWHM of the peak, e.g. Sakai et al. (2000). Instead we use bootstrap resampling of the data (Babu & Feigelson 1996, and references therein) to simulate the act of making the same observation multiple times. This allows for the most realistic estimate of the standard deviation in the mean.

The magnitudes of all the stars brighter than a given limiting magnitide M_l in an entire population have some luminosity function, $\Phi(M > M_l)$. We observe only a random fraction of the whole stellar population and so determine an observed luminosity function, $\hat{\Phi}(M > M_l)$. From this luminosity function we determine I_{TRGB} via either edge detection or maximum likelihood analysis; let us simply refer to the result of either process as $\mathrm{TRGB}(\hat{\Phi})$. We then randomly resample, with replacement, all of the observed magnitudes (i.e., any given star may appear more than once or not at all). Each stellar magnitude, M_i, carries with it some magnitude error, ϵ_i. Thus, during the resampling M_i is perturbed by its errors such that the resampled magnitude, M_i^*, will be randomly drawn from a Gaussian distribution about the original magnitude with ϵ_i as its standard deviation. For each resampling a bootstrap luminosity function , $\hat{\Phi}^*$, is then determined, and I_{TRGB}^* is measured via $\mathrm{TRGB}(\hat{\Phi}^*)$. We perform the bootstrap resampling 500 times for each galaxy and take the standard deviation of the distribution of I_{TRGB}^* as the uncertainty in the measurement of I_{TRGB}. We find that in most cases the estimated uncertainty is a few hundredths to one tenth of one magnitude. Details for each galaxy are given in § 4.3.

4. Distances to Local Galaxies

4.1. TRGB Calibration

With a robust measurement of the I magnitude of the TRGB, I_{TRGB}, we may now calculate the distance modulus. We start with the following equation:

$$(m - M)_I = I_{\mathrm{TRGB}} + BC_I - M_{\mathrm{bol,TRGB}}, \tag{10}$$

where $M_{\mathrm{bol,TRGB}}$ is the bolometric magnitude of the TRGB and BC_I is the bolometric correction to the I magnitude of the TRGB.

The quantity $M_{\mathrm{bol,TRGB}}$ was found by Da Costa & Armandroff (1990, hereafter referred to as DA90) empirically to be a function of the metallicity [Fe/H]:

$$M_{\mathrm{bol,TRGB}} = -0.19[\mathrm{Fe/H}] - 3.81. \tag{11}$$

They also found that BC_I is a function of $(V - I)$ color,

$$BC_I = 0.881 - 0.243(V - I)_{\mathrm{TRGB}}. \tag{12}$$

DA90 determined an empirical relation between $(V - I)$ color and metallicity, but Lee et al. (1993) found it necessary to alter the relation slightly for more distant (and hence fainter) systems, obtaining

$$[\mathrm{Fe/H}] = -12.64 + 12.6(V - I)_{-3.5} - 3.3(V - I)^2_{-3.5}, \tag{13}$$

where $(V - I)_{-3.5}$ is the dereddened red giant branch $(V - I)$ color measured at an absolute I magnitude of -3.5. The absolute magnitude of the TRGB is given by

$$M_{I,\mathrm{TRGB}} = M_{\mathrm{bol,TRGB}} - BC_I. \tag{14}$$

To determine $M_{I,\mathrm{TRGB}}$ we iteratively calculate the distance modulus and the metallicity until they converge. The amount of Galactic extinction (and hence reddening) is calculated for each galaxy using the I and V extinctions given in the NASA/IPAC Extragalactic Database (NED), which are based upon the dust maps of Schlegel et al. (1998).

To measure the $(V - I)$ color of the TRGB, we calculate a histogram of the colors of stars within $I_{\mathrm{TRGB}} \pm 0.1$ mag. We then fit a Gaussian to that histogram (binned at 0.01 mag) and take its peak as a first guess for $(V - I)_{\circ,\mathrm{TRGB}}$. To determine the uncertainty in this value we carry out a bootstrap resampling procedure similar to that used in determination of the uncertainty in I_{TRGB}. Stellar magnitudes and colors are randomly resampled (with replacement) and perturbed by their internal random errors. The histogram calculation and Gaussian fitting are then carried out for each bootstrap resampling (we used 800 bootstrap samples). We fit a Gaussian to the final distribution of $(V - I)_{\circ,\mathrm{TRGB}}$ values and use its peak and standard deviation as the best estimate of $(V - I)_{\circ,\mathrm{TRGB}}$ and its uncertainty. The same procedure is used to determine $(V - I)_{-3.5}$. These values are given for each galaxy in Table 2.

The calibration relations were derived over the metallicity range of the Galactic globular clusters $(-2.1 \leq [\mathrm{Fe/H}] \leq -0.7)$ and are expected to work well over ages spanning 2 - 15 Gyr. The zero point was calibrated to the same level as that of the RR Lyrae distance scale (used to estimate the distances of the Galactic globular clusters). Lee et al. (1993) states generally that for this range $M_{I,\mathrm{TRGB}} \approx -4.0 \pm 0.1$ mag. More specifically, using the above calibration relations and metallicity range one finds $M_{I,\mathrm{TRGB}} = -4.01$ mag with an rms uncertainty of ± 0.03 mag and a systematic error of ± 0.18 mag. Ferrarese et al. (2000b) treated the TRGB as a secondary distance indicator and calibrated a zero point from galaxies with Cepheid distances that yielded $M_{I,\mathrm{TRGB}} = -4.06 \pm 0.07(\mathrm{random}) \pm 0.13(\mathrm{systematic})$ mag. Also, Bellazzini et al. (2001) determined

a new TRGB calibration based on photometry and a distance estimate from a detached eclipsing binary in the Galactic globular cluster ω Centauri. They found $M_{I,\mathrm{TRGB}} = -4.04 \pm 0.12$ mag. For this paper we use the calibration of Lee et al. (1993), but in paper II we will use the calibration of Ferrarese et al. (2000b) for consistency with other recent TRGB measurements.

4.2. Total Error Budget

The true distance modulus for each galaxy is computed as

$$\mu_\circ = (m - M)_I - A_I = I_{\mathrm{TRGB}} - M_{I,\mathrm{TRGB}} - A_I. \tag{15}$$

We consider total errors in distance to be of two forms for these data. There are internal errors that are specific to each galaxy and external systematic errors that are the same for all galaxies. The internal uncertainties in our distances are determined as the sum in quadrature of random and internal systematic errors. The random errors in the distance moduli are taken as the quadrature sum of the random error in measuring I_{TRGB} (estimated via bootstrap resampling) and $M_{I,\mathrm{TRGB}}$ as such

$$(\sigma_{\mu_\circ,\mathrm{random}})^2 = (\sigma_{\mathrm{TRGB,bootstrap}})^2 + (\sigma_{BC_I,\mathrm{random}})^2 + (\sigma_{M_{bol},\mathrm{random}})^2. \tag{16}$$

Uncertainties in $M_{I,\mathrm{TRGB}}$ arise from the errors in measuring the $(V - I)_\circ$ color at I_{TRGB} and at $M_I = -3.5$ as described in the previous section. These errors are propagated through the calibration equations (11-14) :

$$\sigma_{BC_I,\mathrm{random}} = 0.243\sigma_{(V-I)_{0,\mathrm{TRGB}},\mathrm{bootstrap}}, \tag{17}$$

$$\sigma_{M_{bol},\mathrm{random}} = 0.19\sigma_{[\mathrm{Fe/H}]}, \tag{18}$$

and

$$\sigma_{[\mathrm{Fe/H}]} = |12.6 - 6.6(V - I)_{-3.5}|\sigma_{(V-I)_{-3.5},\mathrm{bootstrap}}. \tag{19}$$

Internal systematic errors include the uncertainties in the aperture corrections, the normalization to the standard photometric system (*i.e.* the photometric zero points), and the foreground extinction and reddening . Thus, we have

$$(\sigma_{\mu_\circ,\mathrm{int,sys}})^2 = (\sigma_{I,\mathrm{sys}})^2 + (\sigma_{M_{I,\mathrm{TRGB}},\mathrm{int,sys}})^2 + (\sigma_{A_I})^2, \tag{20}$$

$$\sigma_{M_{I,\mathrm{TRGB}},\mathrm{int,sys}} = (0.243 - 0.19(12.6 - 6.6(V - I)_{-3.5}))\sigma_{(V-I),\mathrm{sys}}, \tag{21}$$

and

$$(\sigma_{(V-I),\mathrm{sys}})^2 = (\sigma_{I,\mathrm{sys}})^2 + (\sigma_{V,\mathrm{sys}})^2 + (\sigma_{E(V-I)})^2. \tag{22}$$

The systematic magnitude errors ($\sigma_{I,\mathrm{sys}}$ and $\sigma_{V,\mathrm{sys}}$) are the quadrature sums of the aperture and zero point corrections in each bandpass. The uncertainties in extinction (A_I) and reddening ($E(V-I) = (A_V - A_I)$) are taken to be 10% of their values (as per Schlegel et al. (1998)).

The values of $\sigma_{\mathrm{TRGB,bootstrap}}$ range from ± 0.02 mag (Sextans B and UGC 06456 using the Maximum Likelihood Method) to ± 0.12 mag (Leo I and UGC 03755 using the Edge Detection Method). The values of $\sigma_{M_{I,\mathrm{TRGB}}}$ range from ± 0.02 mag to ± 0.04 mag. For galaxies without observations in V we use the full range of color/metallicity under which the calibrations were determined. This yields an rms uncertainty of ± 0.03 mag. The total internal uncertainties in the true distance moduli are thus

$$(\sigma_{\mu_\circ,\mathrm{internal}})^2 = (\sigma_{\mu_\circ,\mathrm{random}})^2 + (\sigma_{\mu_\circ,\mathrm{int,sys}})^2, \tag{23}$$

ranging from ± 0.04 mag (Sextans B and UGC 06456 using the Maximum Likelihood Method) to ± 0.13 mag (Leo I and UGC 03755 using the Edge Detection Method).

The principle identified external systematic errors in the determination of the distance moduli arise from the uncertainty in the RR Lyrae distance scale for globular clusters (± 0.15 mag; see Sakai & Madore (1999)), and the uncertainty in the TRGB calibration relations (± 0.11 mag):

$$(\sigma_{\mu_\circ,\mathrm{ext,sys}})^2 = (\sigma_{M_{I,\mathrm{TRGB}},\mathrm{ext,sys}})^2 = (\sigma_{\mathrm{RRLyrae}})^2 + (\sigma_{BC_I,\mathrm{sys}})^2 + (\sigma_{M_{bol},\mathrm{sys}})^2. \tag{24}$$

Da Costa & Armandroff (1990) give the dispersion in equation (12) as ± 0.057 mag and the dispersion in equation (11) as ± 0.09 mag. Thus, the total systematic error common to all our TRGB distance measurements is ± 0.18 mag.

4.3.   TRGB Distances

In order to gain confidence in our photometry and TRGB detection methodology we observed a few local galaxies with Keck that have been studied quite extensively by previous authors, including Leo I, NGC 3109, and Sextans B. We find that our derived distance moduli for these galaxies are in excellent agreement with those of previous authors. In our HST dataset we were able to successfully detect the TRGB for three galaxies and possibly a fourth. The definite detections were UGC 07577, UGC 06456, and NGC 1313, and the possible detection was UGC 03755. There were several galaxies in our combined Keck/*HST* dataset, such as NGC 2366 and NGC 2683, for which we were unable to successfully determine distances . Based upon distance estimates by previous authors using various methods we believe that these galaxies are sufficiently far away that their red giant branch stars were not resolved in our data. A summary of TRGB distances and uncertainties is presented in Table 2. Color-Magnitude diagrams (CMDs), luminosity functions, and other details for these galaxies are now presented. [10]

---

[10]Photometry data for the galaxies presented here are archived in the NED/LEVEL5 database at the following URL: http://nedwww.ipac.caltech.edu/level5/March02/Mendez/.

4.3.1. Leo I

The dwarf spheroidal galaxy Leo I is thought to be one of the most distant satellites of the Milky Way. Our observations with Keck were able to fully resolve Leo I into stars down to $I \sim 24$ mag (See Fig. 2). The Color-Magnitude diagram for the entire field reveals a very simple stellar population of red giants (Fig. 3). There appear to be almost no blue stars that may contaminate the luminosity function. The Red Giant Branch is extremely well defined with an unambiguous tip at $I = 18.14$ mag. Plotted in Fig. 3 is an red giant branch locus for Leo I. We determine this locus by using the value of $(V - I)_{0,\text{TRGB}}$ to interpolate between the two nearest of the four galactic globular cluster loci determined by DA90: M15, M2, NGC 1851, and 47 Tuc. The few stars above the tip are likely Asymptotic Giant Branch (AGB) stars. Also visible is the red clump of helium burning stars at $(V - I)_{\circ} \sim 0.5 - 0.9$ mag and $21.0 \leq I \leq 22.0$ mag.

Fig. 4 shows the logarithmic luminosity function for all stars with $0.3 \leq (V - I) \leq 1.5$ mag. The upper red giant branch power law is quite obvious and has a clear break. Both the maximum likelihood model and the modified Sobel edge detector agree on the location of the break. For the maximum likelihood analysis we determine $I_{\text{TRGB}} = 18.14$ mag as shown in Fig 5. Bootstrap re-sampling gives an uncertainty of ± 0.07 mag, with a distribution shown in Fig. 4. The edge–detector also finds $I_{\text{TRGB}} = 18.14$ mag with a bootstrap uncertainty of ± 0.11 mag. These uncertainties are among the largest of the galaxies reported in this paper, despite Leo I being the closest by far. The large uncertainty is due to the small number of stars at the TRGB. With so few stars at the TRGB it is easier for it to move by a few hundredths of a magnitude with each bootstrap. Madore & Freedman (1995) studied the effect of small population sizes and estimated that if more than ~ 100 stars can be imaged in the first full magnitude interval then any systematic effect in the distance modulus would be well less than 0.1 mag. There are just over 100 stars in the first magnitude of the luminosity function of Leo I. Thus, using the method described in § 4.1 we find $(V - I)_{0,\text{TRGB}} = 1.39 \pm 0.02$ mag and $[\text{Fe/H}] = -1.94 \pm 0.08$ dex. With a line of sight extinction of $A_I = 0.07$ mag we find $(m - M)_I - A_I = \mu_{\circ} = 22.05 \pm 0.10(\text{internal}) \pm 0.18(\text{systematic})$ mag for the maximum likelihood case. This is in excellent agreement with a previously published distance modulus for Leo I of $(m - M)_V = 22.00 \pm 0.15$ mag (Caputo et al. 1999). Another estimate of the TRGB for Leo I was made by Lee et al. (1993), who found $I_{\text{TRGB}} = 18.25 \pm 0.1$ mag (yielding $\mu_{\circ} = 22.18 \pm 0.11$ mag for the assumed $A_I = 0.04$ mag). The difference between their measurement of I_{TRGB} and that presented here is 0.11 ± 0.13 mag, again in good agreement.

4.3.2. Sextans B

Sextans B is a dwarf irregular galaxy located at the edge of the Local Group. It was well resolved in our Keck observations. Fig. 6 shows the CMD for the $\sim 20,000$ resolved stars with good photometry in the LRIS field. The stellar population appears fairly simple; the red giant branch is quite prominent and red giants clearly dominate the light of the galaxy. There is little

contamination from blue stars. The stars above the red giant branch are likely AGB stars that do not obscure the conspicuous TRGB. In order to minimize these contaminants and those arising from crowding and photometric errors we examined the CMD of only the stars in an arbitrary halo region. Fig. 7 shows the positions of the 9500 stars in this halo region and their CMD. The TRGB was already obvious in Fig. 6 but it can now be seen more clearly.

Additionally, we make a color cut in the halo star list. Fig. 8 shows the resulting luminosity function of halo stars with $0.6 \leq (V - I) \leq 1.6$ mag. Again, the power-law distribution with index $a = 0.3$ is evident and has an unambiguous break at $I_{\mathrm{TRGB}} = 21.68$ mag in the maximum likelihood analysis as shown in Fig. 9 (also $I_{\mathrm{TRGB}} = 21.68$ mag in the edge-detector). Bootstrap resampling of stars in the color-cut halo region gives an uncertainty of ± 0.02 mag, shown in panels 3 and 4 of Fig. 8. The TRGB color is estimated to be $(V - I)_{0,\mathrm{TRGB}} = 1.44 \pm 0.01$ mag and the metallicity is $[\mathrm{Fe/H}] = -1.73 \pm 0.04$ dex. The Schlegel et al. (1998) dust maps give the foreground extinction as $A_I = 0.062$ mag. We assume that internal extinction is negligible as we are focusing on the halo region that is presumably mostly dust-free. Thus for the maximum likelihood method we determine a Population II distance modulus of $(m - M)_{\circ} = 25.63 \pm 0.04(\mathrm{internal}) \pm 0.18(\mathrm{systematic})$ mag corresponding to a heliocentric metric distance of 1.34 ± 0.02 Mpc. This result is in superb agreement with a previously published study of Sextans B by Sakai et al. (1997) using both the TRGB $((m - M)_{\circ} = 25.56 \pm 0.10)$ and Cepheids $((m - M)_{\circ} = 25.69 \pm 0.27$ mag).

4.3.3. **NGC 3109**

NGC 3109 is another dwarf irregular galaxy, classified Sm IV, at the edge of the Local Group. It has a flattened disk region apparently viewed nearly edge-on. Our Keck observations have brilliantly resolved the galaxy into stars. In Fig. 10 we present the CMD for the entire LRIS field. This CMD is considerably more complex than those of Sextans B or Leo I. A red giant branch is evident but there is large contamination from blue main sequence and asymptotic giant branch stars. There are also likely some red supergiants in the mix to further complicate matters.

As we did with Sextans B, we selected stars from a halo region to reduce contamination around the TRGB. The pixel map and CMD for these stars is shown in Fig. 11. The red giant branch is now much more apparent as is its tip. The luminosity function of halo stars with $0.7 \leq (V - I) \leq 1.6$ mag is shown in Fig. 12. The two TRGB detection methods agree quite well and we find $I_{\mathrm{TRGB}} = 21.63 \pm 0.05$ mag for the maximum likelihood analysis, as shown in Fig. 13, and $I_{\mathrm{TRGB}} = 21.60 \pm 0.08$ mag for the logarithmic edge–detector. The best estimate of the TRGB color is $(V - I)_{0,\mathrm{TRGB}} = 1.46 \pm 0.02$ mag, with $[\mathrm{Fe/H}] = -1.69 \pm 0.06$ dex. For the maximum likelihood method and using an extinction value of $A_I = 0.129$ mag we find the distance modulus $(m - M)_{\circ} = 25.52 \pm 0.06(\mathrm{internal}) \pm 0.18(\mathrm{systematic})$ mag, which corresponds to a distance from the Sun of 1.27 ± 0.04 Mpc. This is within the errors of a previously published work on NGC 3109 (Minniti et al. 1999) which found $(m - M)_{\circ} = 25.62 \pm 0.1$ mag using the tip of the red giant branch.

4.3.4. **UGC 07577**

The dwarf irregular galaxy UGC 07577 was one of our *HST* target galaxies. Based on our experience with the Keck data we decided to minimize *HST* observation time by only obtaining images in the FW814 filter. This was done for galaxies not expected to have considerable contamination from blue main sequence or asymptotic giant branch populations. Even a large AGB population is not likely to affect the TRGB detection severely as it would surely have a different power-law slope in I band from the red giant branch, so the break in the red giant branch power-law at the TRGB would remain.

The galaxy was well resolved into stars (see Fig. 14). The galaxy (transformed into standard Cousins I) was broken up into core and halo regions as was done for the Keck objects. The luminosity functions of the entire field and of the halo are shown in Fig. 15, and Fig. 16 respectively. All show the same familiar red giant branch power-law slope, $a = 0.3$. The likelihood function for the entire field is maximized at $I_{TRGB} = 23.05 \pm 0.03$ mag and the edge detector gives $I_{TRGB} = 23.01 \pm 0.09$ mag. For the halo region the likelihood function is maximized at $I_{TRGB} = 23.01 \pm 0.06$ mag as shown in Fig. 17 and this is the value we adopt. We assume that the mean metallicity of the UGC 07577 red giants is within the calibrated range of the Galactic globular clusters. Thus we adopt an absolute magnitude of $M_{I,TRGB} = -4.01 \pm 0.03$ mag. Using the maximum likelihood value and an extinction of $A_I = 0.039$ mag we derive a distance modulus for UGC 07577 of $(m - M)_\circ = 26.98 \pm 0.05$(internal)$\pm 0.07$(systematic) mag, which is a heliocentric distance of 2.49 ± 0.08 Mpc. UGC 07577 has been little studied previously, but one recent estimate by Tikhonov & Karachentsev (1998) gives the distance as 4.8 Mpc. This is extremely discrepant, However they were estimating the distance using the magnitudes of the brightest blue super giant stars. Several authors have commented on the errors associated with this method, e.g. Rozanski & Rowan-Robinson (1994); Karachentsev & Tikhonov (1994); Lyo & Lee (1997). While there have been differences between their estimates the errors are generally uncomfortably large (~ 0.79 mag for the brightest blue stars).

4.3.5. **NGC 1313**

NGC 1313 is classified as a SB(s)d barred spiral and was described by de Vaucouleurs (1963) as a transition object from the normal barred spirals to the irregular Magellanic type barred spirals. It has considerable ongoing star formation and an active nucleus. Certainly the mixed stellar populations and the internal extinction of the disk are cause for concern in making a clear distance measurement based on the TRGB. For these reasons we obtained *HST* observations in the halo region of this galaxy 3.67 arcmin from its center (see Fig. 18). In this region we expect the dominant stars to be Population II red giants.

We obtained images only in the F814W bandpass for NGC 1313 as we expected little contamination from other stellar types in this region of the galaxy. In Fig. 19 we present the I band

luminosity function for the entire WFPC2 field of view. The tell-tale power-law signature ($a = 0.3$) of the red giant branch is visible from $I \sim 24.3$ mag down to the photometric limits at $I = 25.5$ mag. While there are many stars brighter than $I \sim 24.3$ mag they would appear to cause little doubt that the red giant branch terminates there. The maximum likelihood analysis gives the magnitude of the TRGB for NGC 1313 as $I_{\mathrm{TRGB}} = 24.28 \pm 0.04$ mag, as shown in Fig. 20, and the modified Sobel edge–detector gives $I_{\mathrm{TRGB}} = 24.35 \pm 0.05$ mag. Since we do not have color information for the NGC 1313 halo we assume that its metallicity is within the calibrated range and thus use $M_{\mathrm{I,TRGB}} = -4.01 \pm 0.03$ mag. Using the maximum likelihood value and the Schlegel et al. (1998) extinction of $A_I = 0.212$ mag we obtain a Population II distance modulus for NGC 1313 of $(m-M)_\circ = 28.08 \pm 0.06 \text{(internal)} \pm 0.18 \text{(systematic)}$ mag corresponding to a heliocentric distance of 4.13 ± 0.11 Mpc. Using the magnitudes of brightest resolved stars, de Vaucouleurs (1963) estimated the distance of NGC 1313 at 4.5 Mpc. Tully (1988) additionally gives the distance to NGC 1313 as 3.7 Mpc.

4.3.6. **UGC 06456**

In addition to our own *HST* data we searched through the *HST* archive at STScI for WFPC2 observations of galaxies in our all sky sample in at least F814W. While we found several good candidates, most of the observations we found were for disk regions within spiral galaxies. We have found at least one excellent dataset to add to our study. The observations (program 6276, PI J. Westphal) were taken as part of a project to study peculiar and interacting galaxies. From the archive data we used three 1400s exposures in F555W and three 1400s exposures in F814W of the blue compact dwarf galaxy (BCD) UGC 06456. We reduced these data as described in § 2.2 for our own *HST* observations.

The observations resolved the galaxy brilliantly into stars revealing a bright and knotted population of blue stars at its core and a smooth background of red stars. Fig. 21 shows our color-magnitude diagram for the entire WFPC2 field. Evident in the CMD is a strong population of blue main sequence stars as well as a prominent red giant branch. There are also a small number of AGB stars visible above the red giant branch. We were able to remove the contamination from the blue stars by excluding the stars from the central region as shown in Fig. 22. Furthermore we exclude stars with colors outside the range $0.45 \leq (V - I) \leq 1.8$ mag. Fig. 23 shows the resulting luminosity function.

The TRGB is extremely obvious and the maximum likelihood analysis finds the TRGB at $I_{\mathrm{TRGB}} = 24.23 \pm 0.02$ mag, as shown in Fig. 24, and the color of the TRGB is $(V-I)_{0,\mathrm{TRGB}} = 1.46 \pm 0.02$ mag. We thus take the metallicity of the red giant branch to be $[\mathrm{Fe/H}] = -1.62 \pm 0.05$. Using an extinction of $A_I = 0.070$ mag we find the distance modulus for UGC 06456 to be $(m - M)_\circ = 28.19 \pm 0.04 \text{(internal)} \pm 0.18 \text{(systematic)}$ mag and hence the heliocentric distance to be 4.34 ± 0.07 Mpc. This is in good agreement with the TRGB analysis carried out by previous authors using these same data (Lynds et al. 1998; Schulte-Ladbeck et al. 1998) who found $(m-M)_I = 28.25 \pm 0.10$

and $(m - M)_\circ = 28.4 \pm 0.09 \pm 0.18$ mag respectively.

4.3.7. **UGC 03755**

UGC 03755 is a typical dwarf irregular galaxy that has been little studied by previous authors. It was of particular interest to us because it lies in the region of the sky with the strongest predicted infall (see Fig. 1).

Fig. 25 shows one of our F814W exposures of UGC 03755. The galaxy appears well resolved into stars. However, inspection of the CMD (Fig. 26) shows that we did not resolve the galaxy very deeply, especially in the F555W bandpass. There is only the slightest hint of a red giant branch, and the F555W photometry limits cut into it almost immediately. Making region or color cuts does not actually help a detection in this case. However, upon inspection of the luminosity function for UGC 03755 (Fig. 27) we can see the red giant branch power-law signature for ~ 0.8 mag brighter than the magnitude limits in I band. There is no strong discontinuity in the luminosity function as seen with the previous galaxies but there is a definite break in the power-law. We interpret this break as the tip of the red giant branch at $I_{\mathrm{TRGB}} = 24.65 \pm 0.06$ mag, as measured weakly by the maximum likelihood algorithm and shown in Fig. 28. Because the red giant branch is not well defined we chose to treat UGC 03755 as a case in which we did not have color data and hence we assume that its metallicity is within the calibrated range and adopt $M_{\mathrm{I,TRGB}} = -4.01 \pm 0.03$ mag. We use the Schlegel et al. (1998) line of sight extinction of $A_I = 0.172$ mag, which yields a distance modulus of $(m - M)_\circ = 28.49 \pm 0.07$(internal)$\pm 0.18$(systematic) mag. This corresponds to a heliocentric distance of 4.98 ± 0.17 Mpc. We take this as a lower limit on the distance to this galaxy, for if it were closer we should have seen a definitive red giant branch. Likewise we take this distance as the upper limit for our ability to measure distances in our *HST* dataset. Since all of our exposure times were the same we would not resolve the red giant branch population of any galaxy that is farther than this.

Georgiev et al. (1997) estimated $(m - M) = 28.08$ mag for this galaxy, based upon the magnitudes of the brightest resolved stars. In another paper (Georgiev et al. 1997) they estimated the calibration errors in their method to be ± 0.39 mag. There is no strong agreement, but again we believe that UGC 03755 cannot be any closer than ~ 5.0 Mpc.

4.3.8. **NGC 2366 & NGC 2683**

With success comes failure; we were not able to determine TRGB distances to many of our target galaxies. Based on our successful measurements and on work done by previous authors, we do not think that our failures were caused by contaminating stellar populations. Rather we think that in most cases the data were simply not deep enough to resolve out red giant branch stars. Hence, the galaxies are too far away for our data to reveal the TRGB.

We estimate that in our Keck data we would not have been able to detect any red giant branch (or tip thereof) fainter than $I \sim 23.0$ mag. We take the limiting magnitude as at least 0.5 magnitudes brighter than the turn over in the luminosity function. This means that we could not have successfully measured a TRGB distance for any galaxy with a distance greater than 2.5 Mpc. This was unfortunate as many of our Keck targets are expected members of the M81 group. One example is NGC 2366. This dwarf irregular galaxy has been estimated to lie at a distance $d \leq 3.44$ Mpc, which is consistent with other M81 group members (Ferrarese et al. 2000a, and references therein). Our CMD for this galaxy (Fig. 29) shows no recognizable structure, and the luminosity function turns over at about $I \sim 23.5$ mag never having any red giant branch power-law slope. Clearly our data for this object did not go deep enough to resolve a red giant branch population.

The situation is much the same for our *HST* data. The typical detection limit in the *HST* data is $I \sim 25.0$ mag, corresponding to a linear distance limit of 6.2 Mpc. An example of a galaxy we failed to measure a TRGB distance for is NGC 2683. This is a spiral galaxy seen nearly edge-on. We avoided the disk region and observed only in the halo region of the galaxy to minimize any Population I contamination. A recent survey of galaxies by Tonry et al. (2001) that used surface brightness fluctuations as a distance indicator gave a distance for this galaxy of 7.7 Mpc. This galaxy is then clearly outside the reach of our data. There is little wonder that we see no hint of a red giant branch power-law in the luminosity function (Fig. 30).

5. Summary

We have successfully used the TRGB as a distance indicator for seven local galaxies observed with *HST* and Keck. Using knowledge of the luminosity function behavior of the red giant branch, we conducted a maximum likelihood procedure to estimate the I band magnitude of the TRGB. The uncertainty in the estimates of I_{TRGB} and $(V - I)_{\mathrm{TRGB}}$ were calculated via bootstrap resampling which makes no assumption about the underlying distributions and allows one to model the act of making repeated measurements of the same quantity. Bootstrap resampling also allows us to better estimate the error in I_{TRGB} when the number of red giant branch stars at that magnitude is small. We find that compared to Sobel edge detection the maximum likelihood analysis is equally accurate but more precise, and we find no systematic difference in the derived values of I_{TRGB} between the two methods. Indeed we find the weighted mean absolute difference in I_{TRGB} to be $< |I_{\mathrm{TRGB,ML}} - I_{\mathrm{TRGB,ED}}| >= 0.03 \pm 0.02$ mag (the simple average absolute difference in I_{TRGB} is $< |I_{\mathrm{TRGB,ML}} - I_{\mathrm{TRGB,ED}}| >= 0.03 \pm 0.01$ mag). The average ratio of uncertainties is $< \sigma_{\mathrm{TRGB,ML}}/\sigma_{\mathrm{TRGB,ED}} >= 0.62$. Therefore, on average, the maximum likelihood method is 38% more precise than the Sobel edge detection. It should also be noted that other authors (e.g. Cioni et al. (2000)) have found Sobel edge detection to be a biased estimator of the TRGB. The bias depends on the amount of smoothing in the luminosity function at the location of the TRGB. For our data this bias was less than 0.04 mag which is less than random errors and therefore we would not be sensitive to it in a comparison to the maximum likelihood. It is a positive feature of the

TRGB method that it does not depend very sensitively on the statistical technique used to define the tip. The TRGB method will be most useful in further broadening our knowledge of distances to local galaxies and allow us to study the local flow in greater detail.

REFERENCES

Babu, G. J., & Feigelson, E. D., ed. 1996, Astrostatistics interdisciplinary statistics

Baker, J. E., Davis, M., Strauss, M. A., Lahav, O., & Santiago, B. . X. 1998, ApJ, 508, 6

Beland, S., Boulade, O., & Davidge, T. 1988, CFHT Info. Bull., 19, 16

Bellazzini, M., Ferraro, F. R., & Pancino, E. 2001, ApJ, 556, 635

Burrows, C. J., ed. 1994, Hubble Space Telescope Wide Field and Planetary Camera 2 Instrument handbook, version 2.0

Burstein, D. 1990, Reports on Progress in Physics, 53, 421

Caputo, F., Cassisi, S., Castellani, M., Marconi, G., & Santolamazza, P. 1999, AJ, 117, 2199

Cioni, M.-R. L., van der Marel, R. P., Loup, C., & Habing, H. J. 2000, A&A, 359, 601

Da Costa, G. S., & Armandroff, T. E. 1990, AJ, 100, 162

de Vaucouleurs, G. 1963, ApJ, 137, 720

Dolphin, A. E. 2000a, PASP, 112, 1397

Dolphin, A. E. 2000b, PASP, 112, 1383

Dolphin, A. E., et al. 2001, MNRAS, 324, 249

Ferrarese, L., et al. 2000a, ApJS, 128, 431

Ferrarese, L., et al. 2000b, ApJ, 529, 745

Fisher, K. B., Davis, M., Strauss, M. A., Yahil, A., & Huchra, J. P. 1994, MNRAS, 267, 927

Georgiev, T. B., Bilkina, B. I., & Dencheva, N. M. 1997, Astronomy Letters, 23, 656

Georgiev, T. B., Karachentsev, I. D., & Tikhonov, N. A. 1997, Astronomy Letters, 23, 514

Holtzman, J. A., et al. 1995, PASP, 107, 156

Iben, I., & Renzini, A. 1983, ARA&A, 21, 271

Karachentsev, I. D., & Makarov, D. A. 1996, AJ, 111, 794

Karachentsev, I. D., & Tikhonov, N. A. 1994, A&A, 286, 718

Kim, M., Kim, E., Lee, M. G., Sarajedini, A., & Geisler, D. 2002, AJ, 123, 244

Krist, J., & Hook, R., ed. 1996, Tiny Tim User's Manual, V4.2

Landolt, A. U. 1992, AJ, 104, 340

Lee, M. G., Freedman, W., Mateo, M., Thompson, I., Roth, M., & Ruiz, M. 1993, AJ, 106, 1420

Lee, M. G., Freedman, W. L., & Madore, B. F. 1993, ApJ, 417, 553

Lynds, R., Tolstoy, E., O'Neil., E. J., & Hunter, D. A. 1998, AJ, 116, 146

Lyo, A.-R., & Lee, M. G. 1997, Journal of Korean Astronomical Society, 30, 27

Madore, B. F., & Freedman, W. L. 1995, AJ, 109, 1645

Madore, B. F., & Freedman, W. L. 1998, in Stellar astrophysics for the local group: VIII Canary Islands Winter School of Astrophysics, 263

Méndez, B., Davis, M., Newman, J., Madore, B. F., Freedman, W. L., & Moustakas, J. 2002, In Preparation

Minniti, D., Zijlstra, A. A., & Alonso, M. V. 1999, AJ, 117, 881

Mould, J., & Kristian, J. 1986, ApJ, 305, 591

Nusser, A., & Davis, M. 1994, ApJ, 421, L1

Oke, J. B., et al. 1995, PASP, 107, 375

Peebles, P. J. E. 1993, Principles of physical cosmology (Princeton Series in Physics, Princeton, NJ: Princeton University Press, —c1993)

Renzini, A., & Fusi Pecci, F. 1988, ARA&A, 26, 199

Rozanski, R., & Rowan-Robinson, M. 1994, MNRAS, 271, 530

Saha, A., Sandage, A., Tammann, G. A., Dolphin, A. E., Christensen, J., Panagia, N., & Macchetto, F. D. 2001, ApJ, 562, 314

Sakai, S., & Madore, B. F. 1999, ApJ, 526, 599

Sakai, S., Madore, B. F., & Freedman, W. L. 1996, ApJ, 461, 713

Sakai, S., Madore, B. F., & Freedman, W. L. 1997, ApJ, 480, 589

Sakai, S., Zaritsky, D., & Kennicutt, R. C. 2000, AJ, 119, 1197

Salaris, M., & Cassisi, S. 1997, MNRAS, 289, 406

Sandage, A., Tammann, G. A., & Yahil, A. 1979, ApJ, 232, 352

Schechter, P. L., Mateo, M., & Saha, A. 1993, PASP, 105, 1342

Schlegel, D. J., Finkbeiner, D. P., & Davis, M. 1998, ApJ, 500, 525

Schulte-Ladbeck, R. E., Crone, M. M., & Hopp, U. 1998, ApJ, 493, L23

Seitzer, P., et al. 2001, in American Astronomical Society Meeting, Vol. 33, 800

Shaklan, S., Sharman, M. C., & Pravdo, S. H. 1995, Appl. Opt., 34, 6672

Stetson, P. B. 1987, PASP, 99, 191

Stetson, P. B. 1994, PASP, 106, 250

Stetson, P. B. 2000, PASP, 112, 925

Tikhonov, N. A., & Karachentsev, I. D. 1998, A&AS, 128, 325

Tonry, J. L., Dressler, A., Blakeslee, J. P., Ajhar, E. A., Fletcher, A. ., Luppino, G. A., Metzger, M. R., & Moore, C. B. 2001, ApJ, 546, 681

Tully, R. B. 1988, Nearby galaxies catalog (Cambridge and New York, Cambridge University Press, 1988, 221 p.)

Udalski, A., Wyrzykowski, L., Pietrzynski, G., Szewczyk, O., Szymanski, M., Kubiak, M., Soszynski, I., & Zebrun, K. 2001, Acta Astronomica, 51, 221

Wyder, T. K. 2001, AJ, 122, 2490

Zoccali, M., & Piotto, G. 2000, A&A, 358, 943
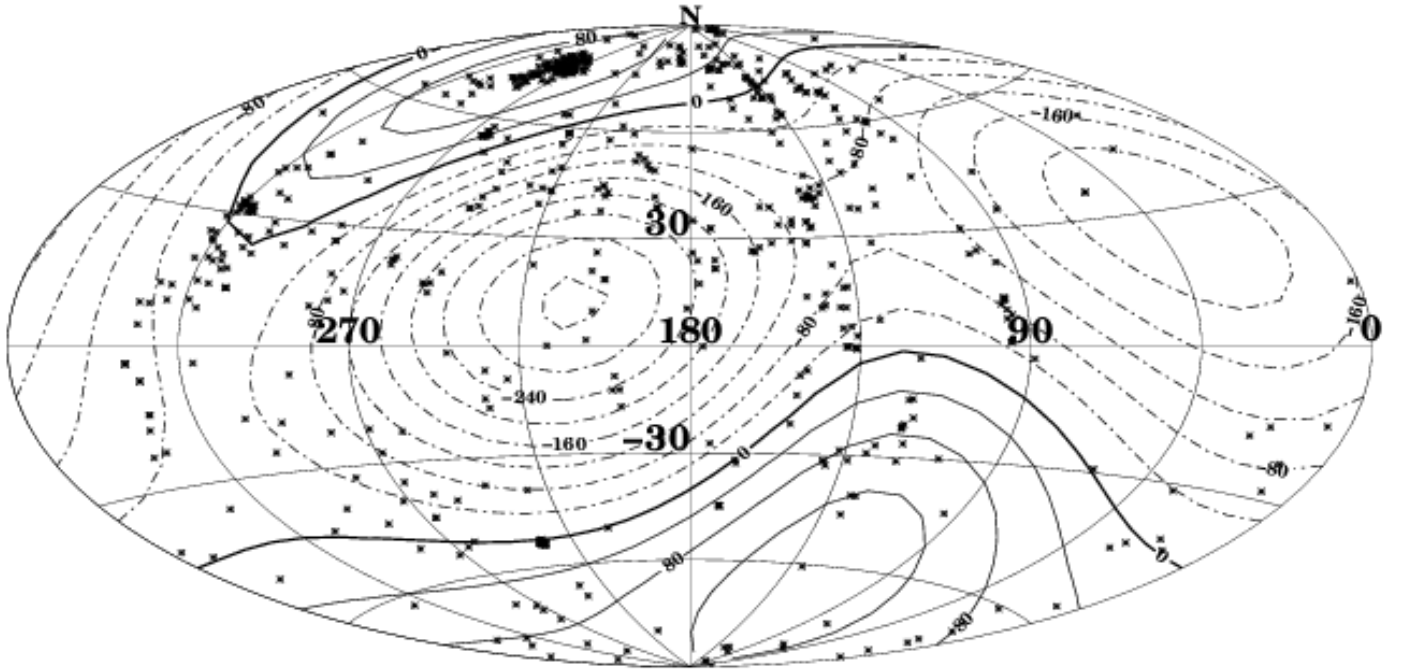
Fig. 1.— Full-sky contour map (in Galactic co-ordinates) of the predicted radial velocity field on a shell at redshift $cz = 500$ km s^{-1} (in the frame of the Local Group) derived from the IRAS galaxy distribution (see Nusser & Davis (1994), for details). Contours are in units of 50 km s^{-1} with the dash–dot lines representing infall peculiar velocity and solid lines representing outflow peculiar velocity. The amplitude of the flow is almost linear in $\beta \equiv \Omega^{0.6}/b_I$, where b_I is the linear bias in the IRAS galaxy distribution relative to the mass distribution. The plot assumes $\beta = 0.6$. Galaxies with $cz < 550$ km s^{-1} are plotted.
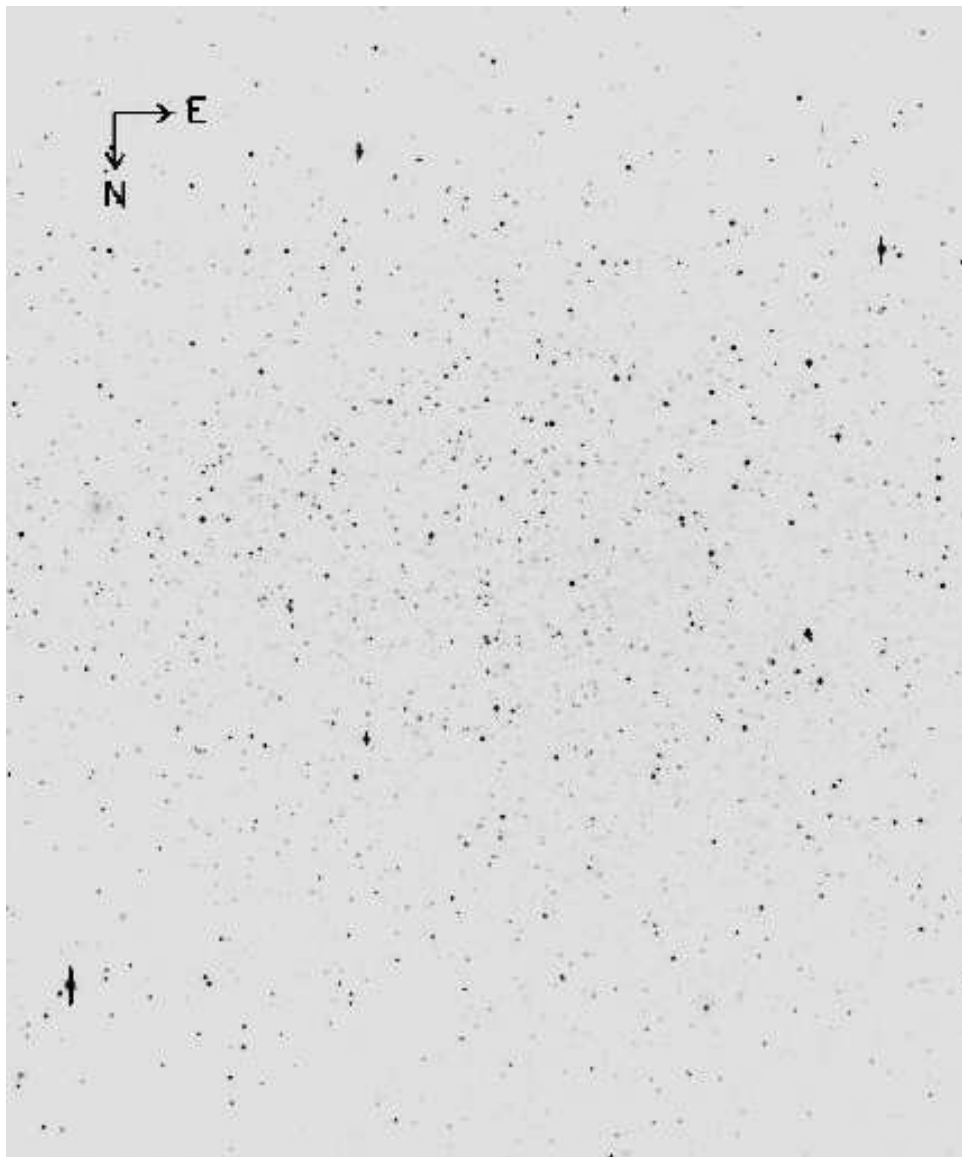
Fig. 2.— Single 300s Keck/LRIS CCD image of Leo I in the I band. The image is 5.5' x 7.3'.
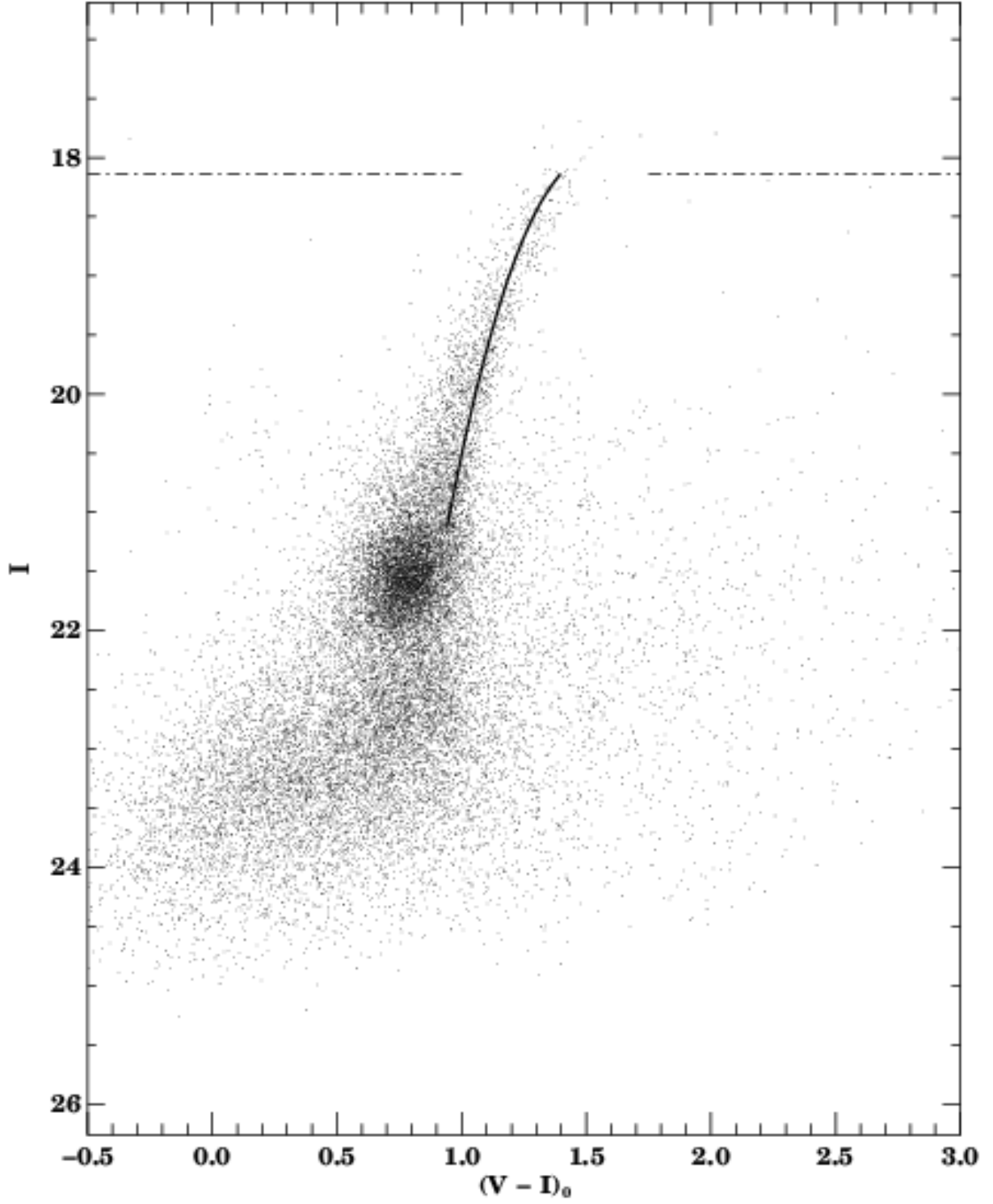
Fig. 3.— Color–Magnitude Diagram for all stars in the Leo I CCD frame. The red giant branch locus (determined as discussed in the text) is also plotted. The $(V - I)$ color has been corrected for foreground reddening using the extinction values given in NED.
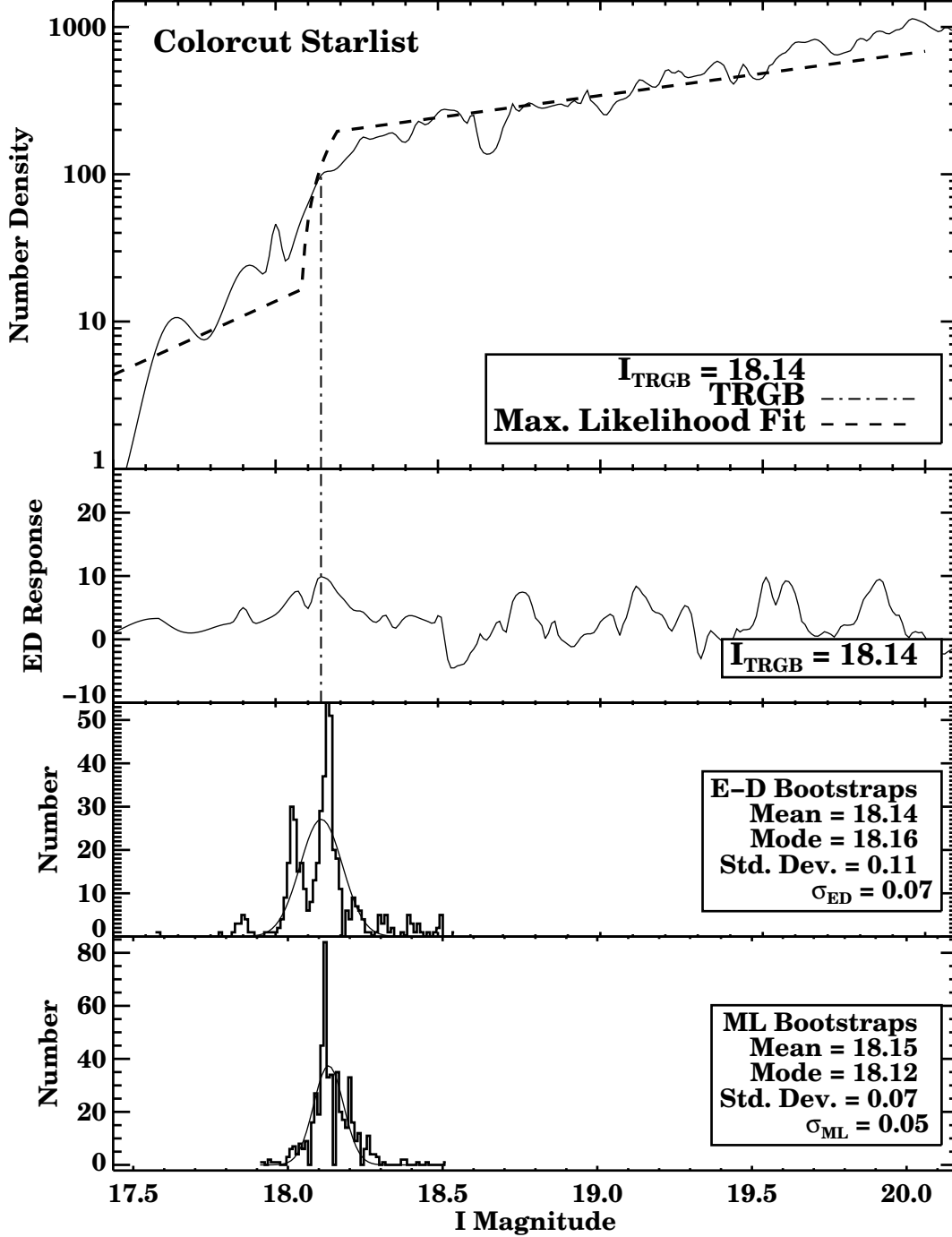
Fig. 4.— Luminosity function of stars in Leo I with $0.3 \leq (V - I) \leq 1.5$ mag (top panel). Over-plotted is the best-fit model luminosity function determined via maximum likelihood analysis. The second panel plots the weighted logarithmic edge–detection response; the dot–dash line indicates the TRGB location. The third and fourth panels plot the distribution of the bootstrap results for edge–detection and maximum likelihood methods, respectively.
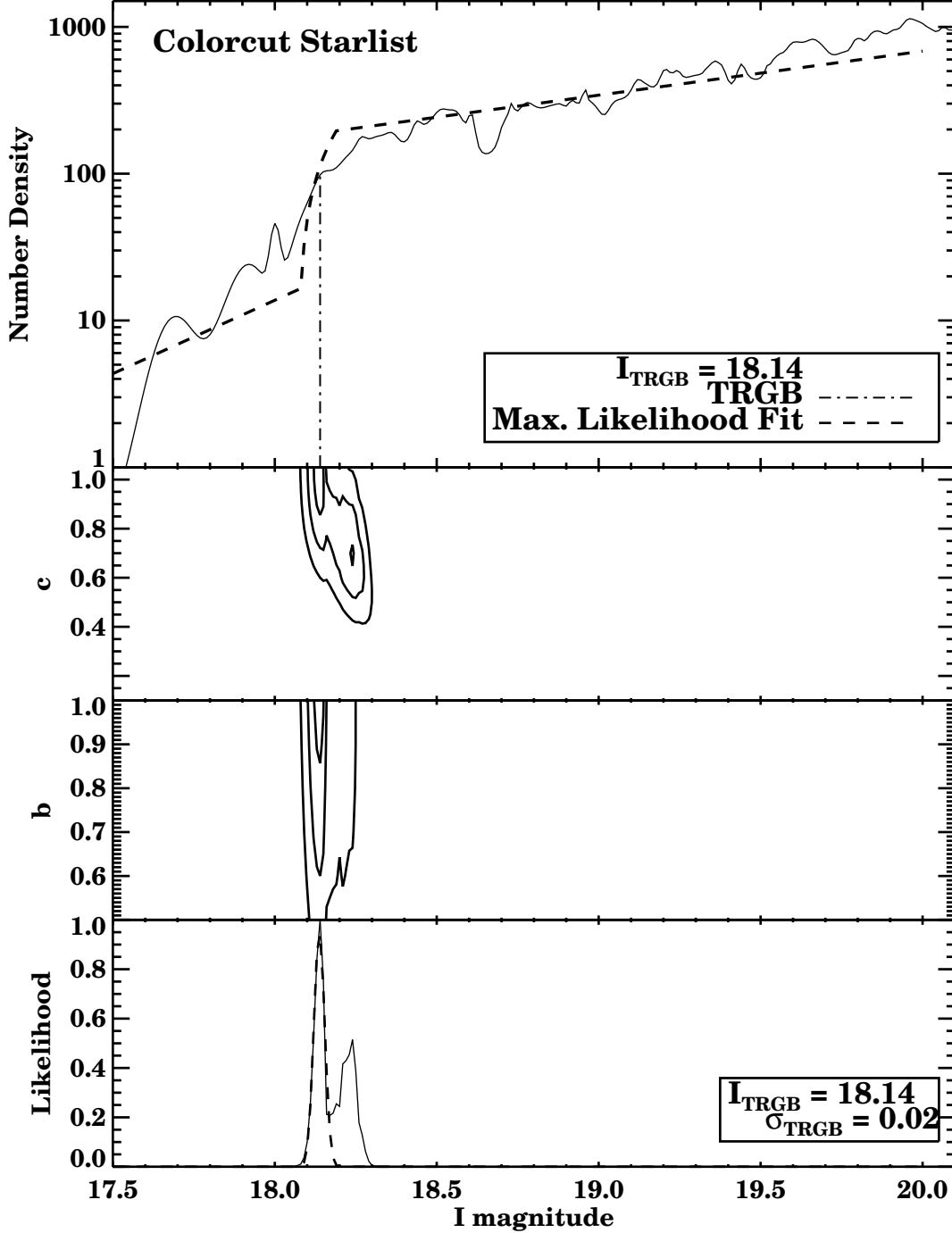
Fig. 5.— Luminosity function of stars in Leo I with $0.3 \leq (V - I) \leq 1.5$ mag (top panel). Overplotted is the best-fit model luminosity function determined via maximum likelihood analysis. The second and third panels plot 1σ, 2σ, and 3σ contours of the likelihood function parameters c and b, respectively. The fourth panel plots the marginalized likelihood. A Gaussian fit with $\sigma_{\mathrm{TRGB}} = 0.02$ mag is overplotted as a dashed line.
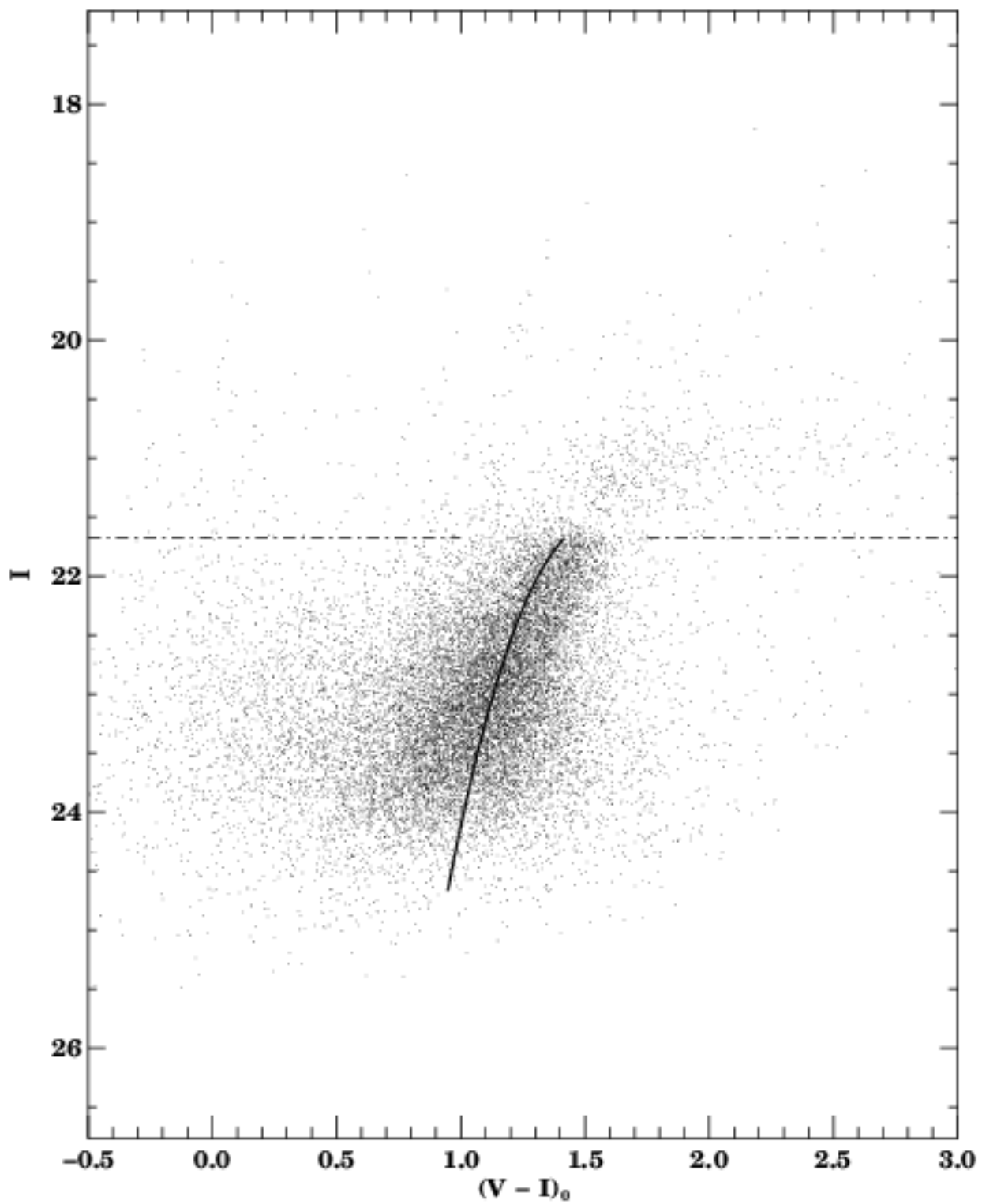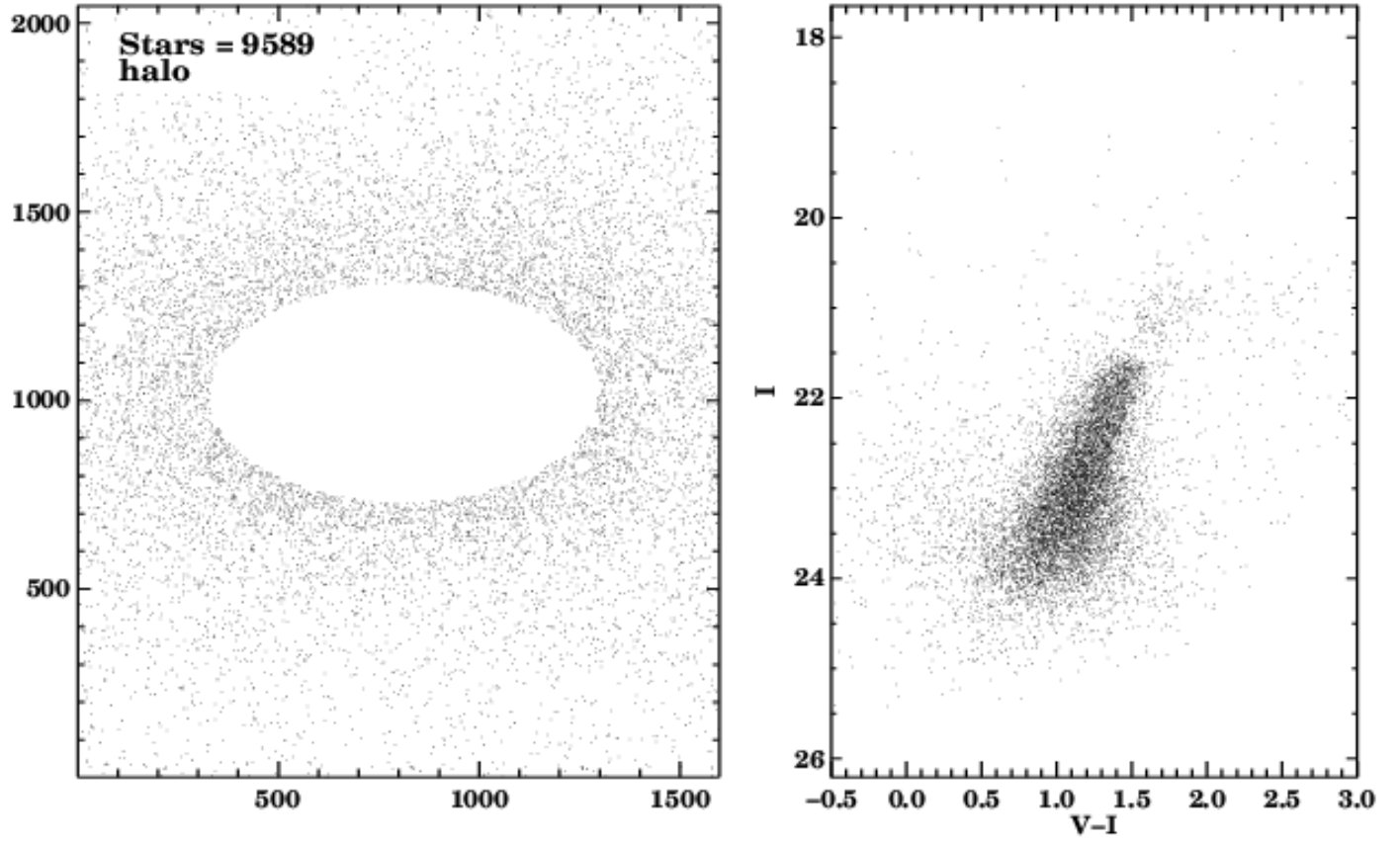
Fig. 6.— Color–Magnitude Diagram for all stars in the Sextans B CCD frame. The red giant branch locus (determined as discussed in the text) is also plotted.

Fig. 7.— The left panel is a map of the pixel positions of all stars in the halo region of Sextans B. The right panel is a Color–Magnitude diagram of just these stars. Notice that the TRGB is more obvious than in Fig. 6 after cutting out the core region.
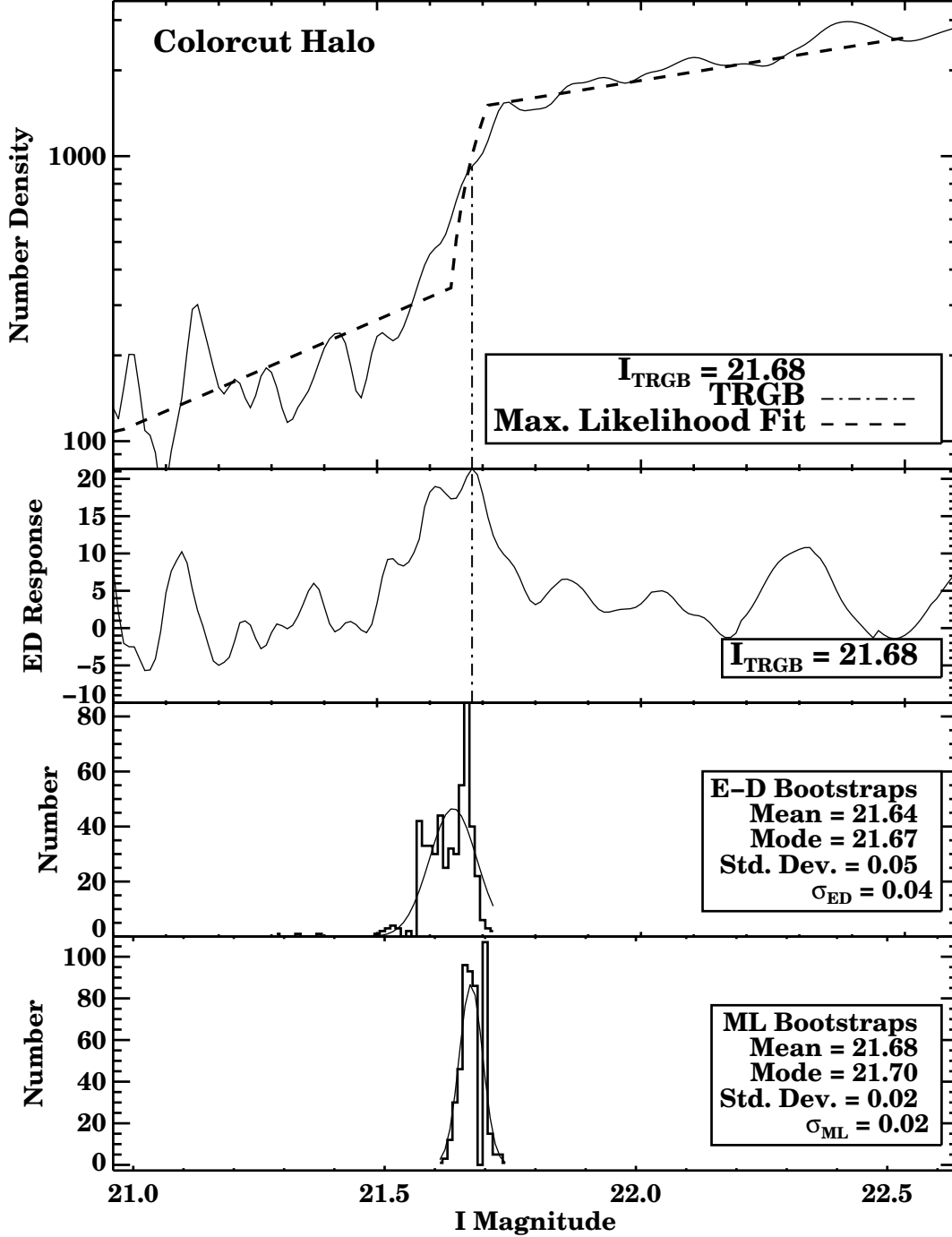
Colorcut Halo

$I_{TRGB} = 21.68$
TRGB — · — ·
Max. Likelihood Fit – – – –

$I_{TRGB} = 21.68$

E–D Bootstraps
Mean = 21.64
Mode = 21.67
Std. Dev. = 0.05
$\sigma_{ED} = 0.04$

ML Bootstraps
Mean = 21.68
Mode = 21.70
Std. Dev. = 0.02
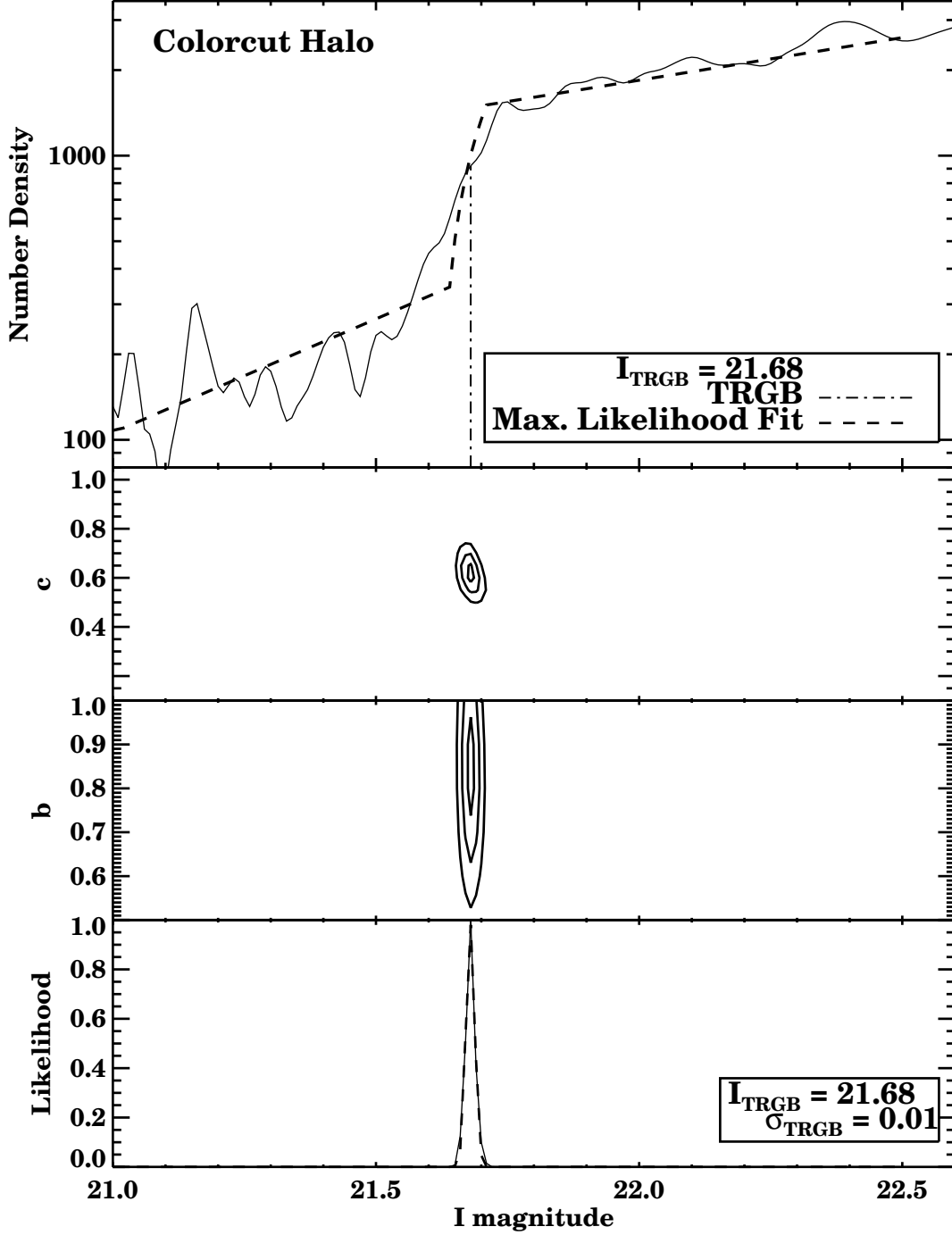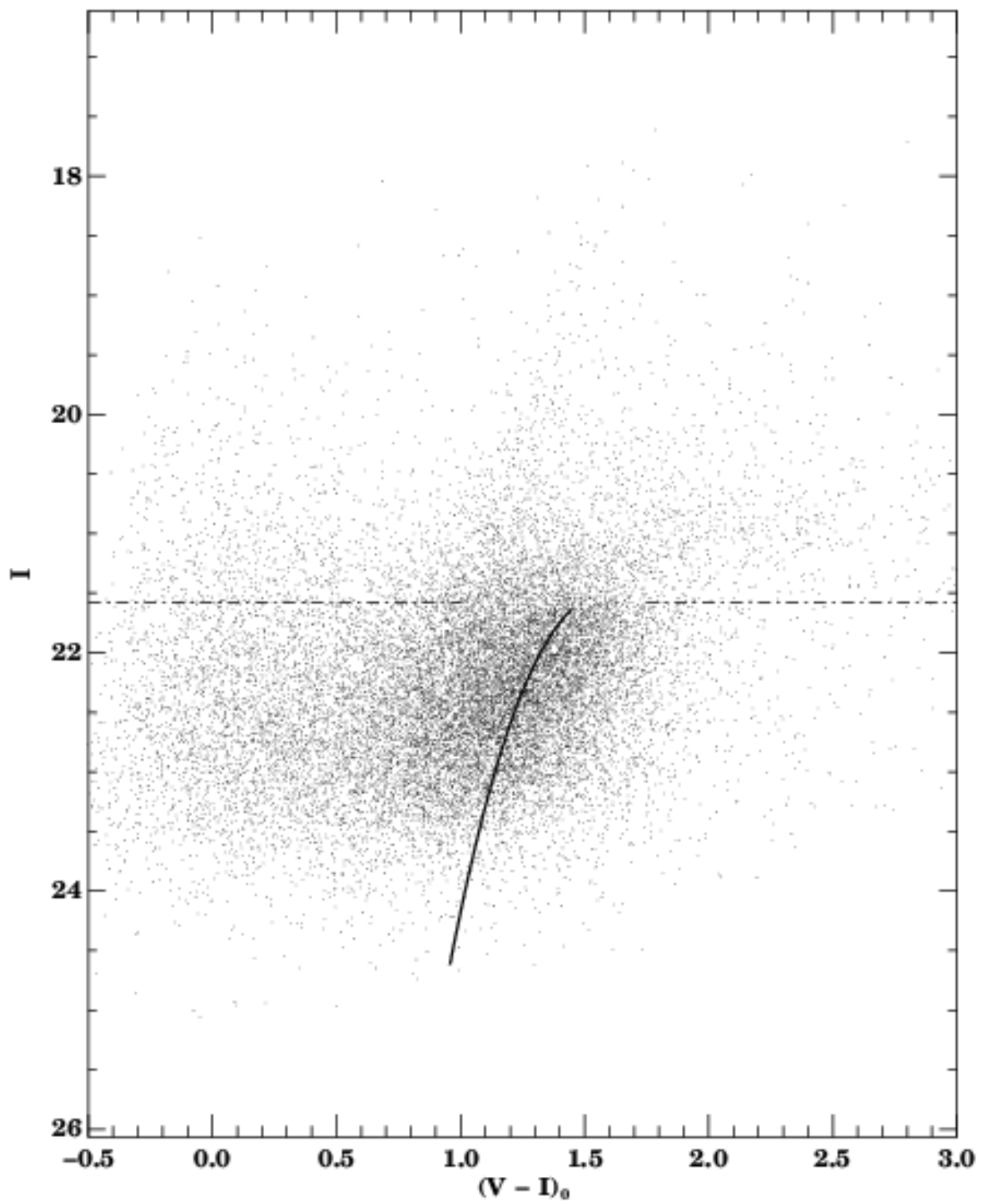$\sigma_{ML} = 0.02$

Fig. 8.— Luminosity function of stars in the halo of Sextans B with $0.6 \leq (V - I) \leq 1.6$ mag (top panel). Overplotted is the best-fit model luminosity function determined via maximum likelihood analysis. The second panel plots the weighted logarithmic edge–detection response with a dot–dash line indicating the TRGB. The third and fourth panels plot the distribution of the bootstrap results for edge–detection and maximum likelihood methods, respectively.

Fig. 9.— Luminosity function of stars in the halo of Sextans B with $0.6 \leq (V - I) \leq 1.6$ mag (top panel). Overplotted is the best–fit model luminosity function determined via a maximum likelihood analysis. The second and third panels plot 1σ, 2σ, and 3σ contours of the likelihood function parameters c and b. The fourth panel plots the marginalized likelihood. A Gaussian fit with $\sigma_{\mathrm{TRGB}} = 0.01$ mag is overplotted as a dashed line.

Fig. 10.— Color–Magnitude Diagram for all stars in the NGC 3109 CCD frame. The red giant branch locus (determined as discussed in the text) is also plotted.
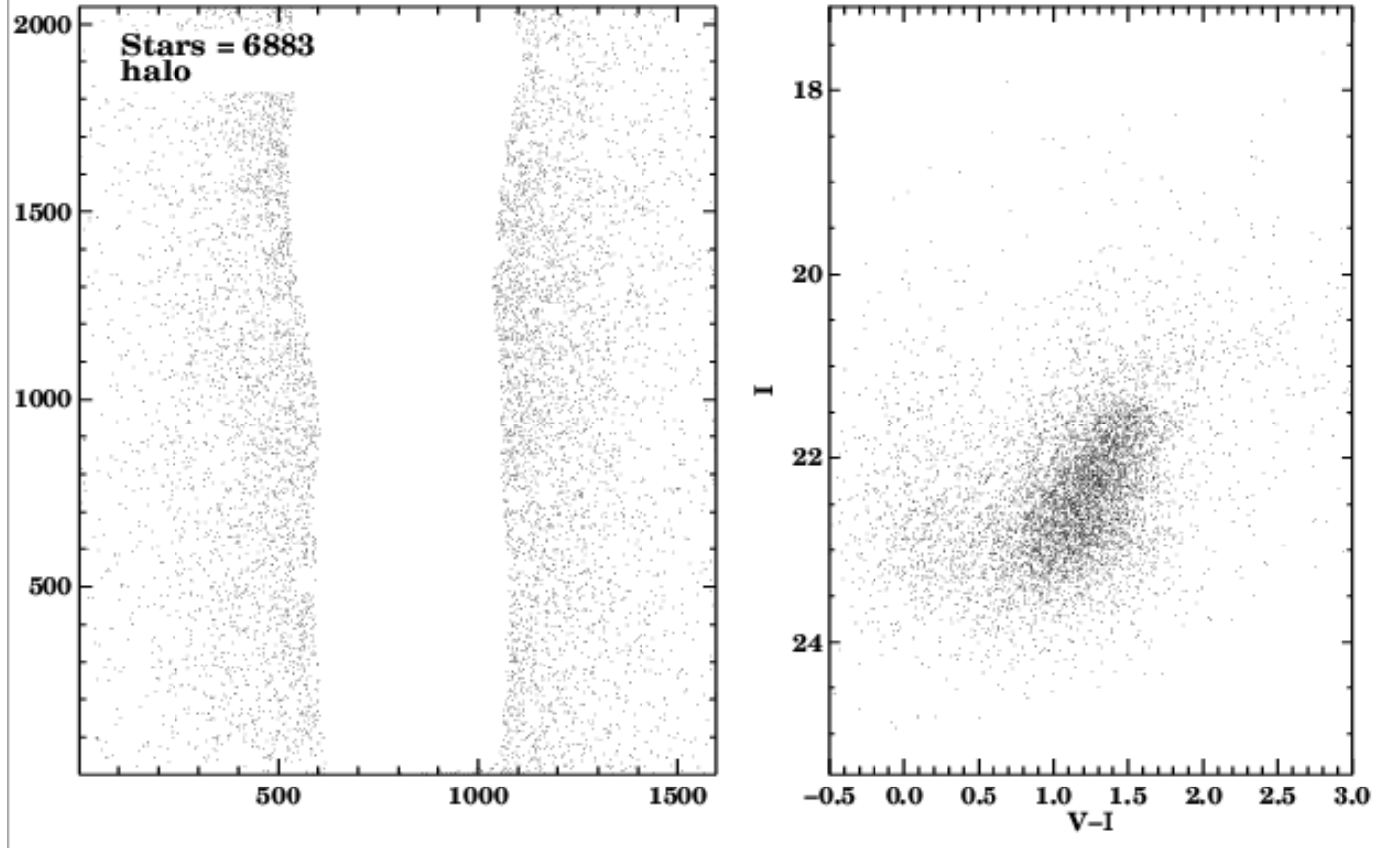
Fig. 11.— The left panel is a map of the pixel positions of all stars in the halo region of NGC 3109. The right panel is a Color–Magnitude diagram of just these stars. Notice that the TRGB is more obvious than in Fig. 10 after cutting out the core region.
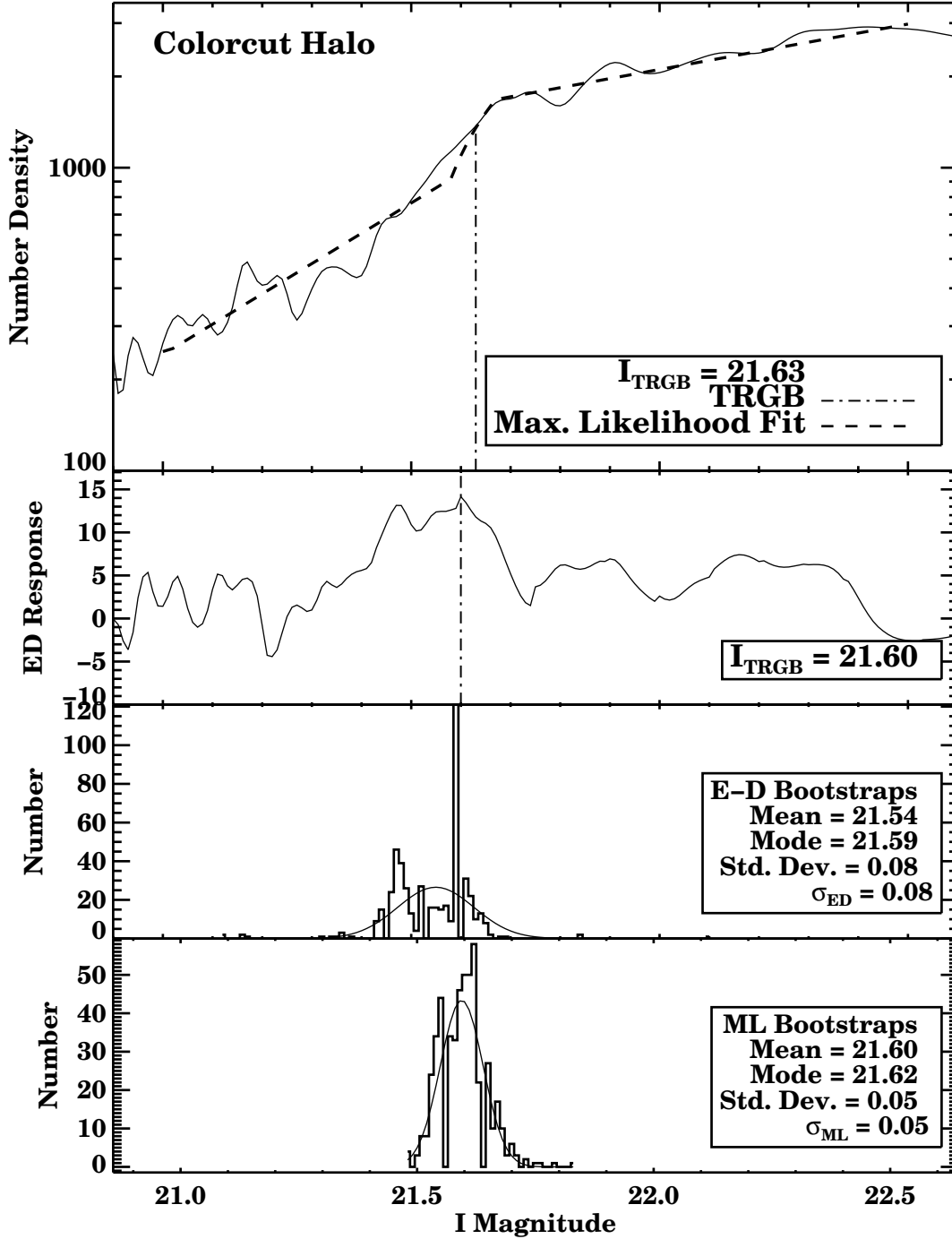
Fig. 12.— Luminosity function of stars in the halo of NGC 3109 with $0.7 \leq (V - I) \leq 1.6$ mag (top panel). Overplotted is the best–fit model luminosity function determined via maximum likelihood analysis. The lower three panels are as in Fig. 4
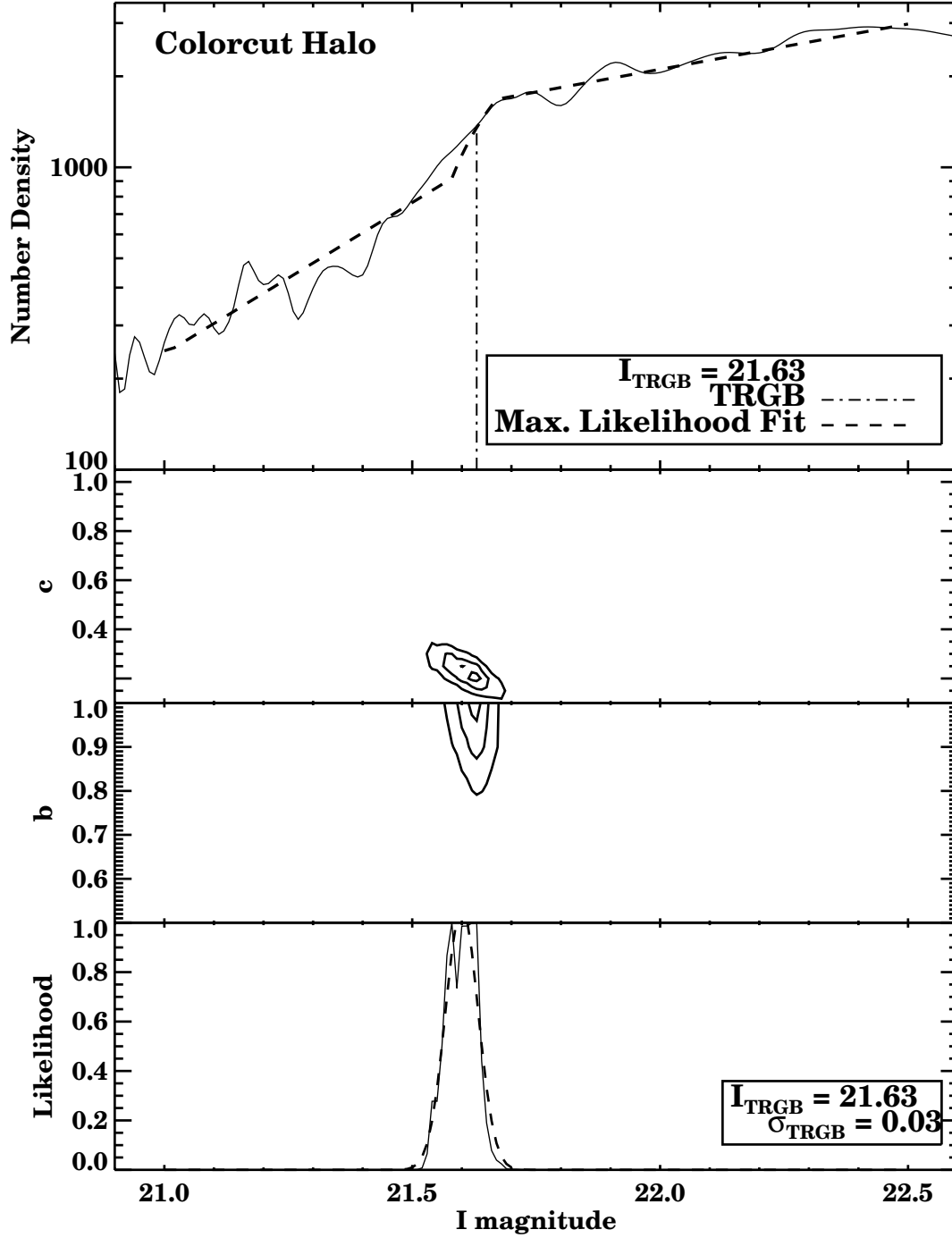
Fig. 13.— Top panel is as in Fig. 12. The second and third panels plot 1σ, 2σ, and 3σ contours of the likelihood function parameters c and b. The fourth panel plots the marginalized likelihood. A Gaussian fit with $\sigma_{\mathrm{TRGB}} = 0.03$ mag is overplotted as a dashed line.
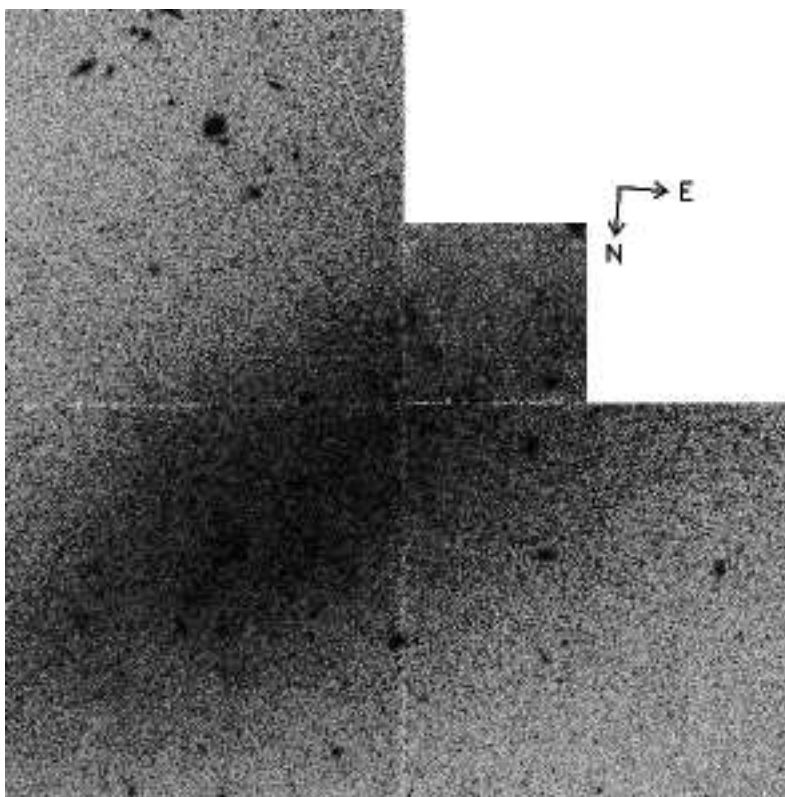
Fig. 14.— Mosaic of a single 1300s *HST*/WFPC2 exposure of UGC 07577.

Whole Starlist

Number Density

1000

I_{TRGB} = 23.05
TRGB — · — · —
Max. Likelihood Fit — — — —

ED Response

20

10

0

−10

I_{TRGB} = 23.01

Number

80

60

40

20

0

E–D Bootstraps
Mean = 23.04
Mode = 23.10
Std. Dev. = 0.05
σ_{ED} = 0.06

Number

120

100

80

60

40

20

0

ML Bootstraps
Mean = 23.06
Mode = 23.04
Std. Dev. = 0.03
σ_{ML} = 0.01

22.5   23.0   23.5   24.0
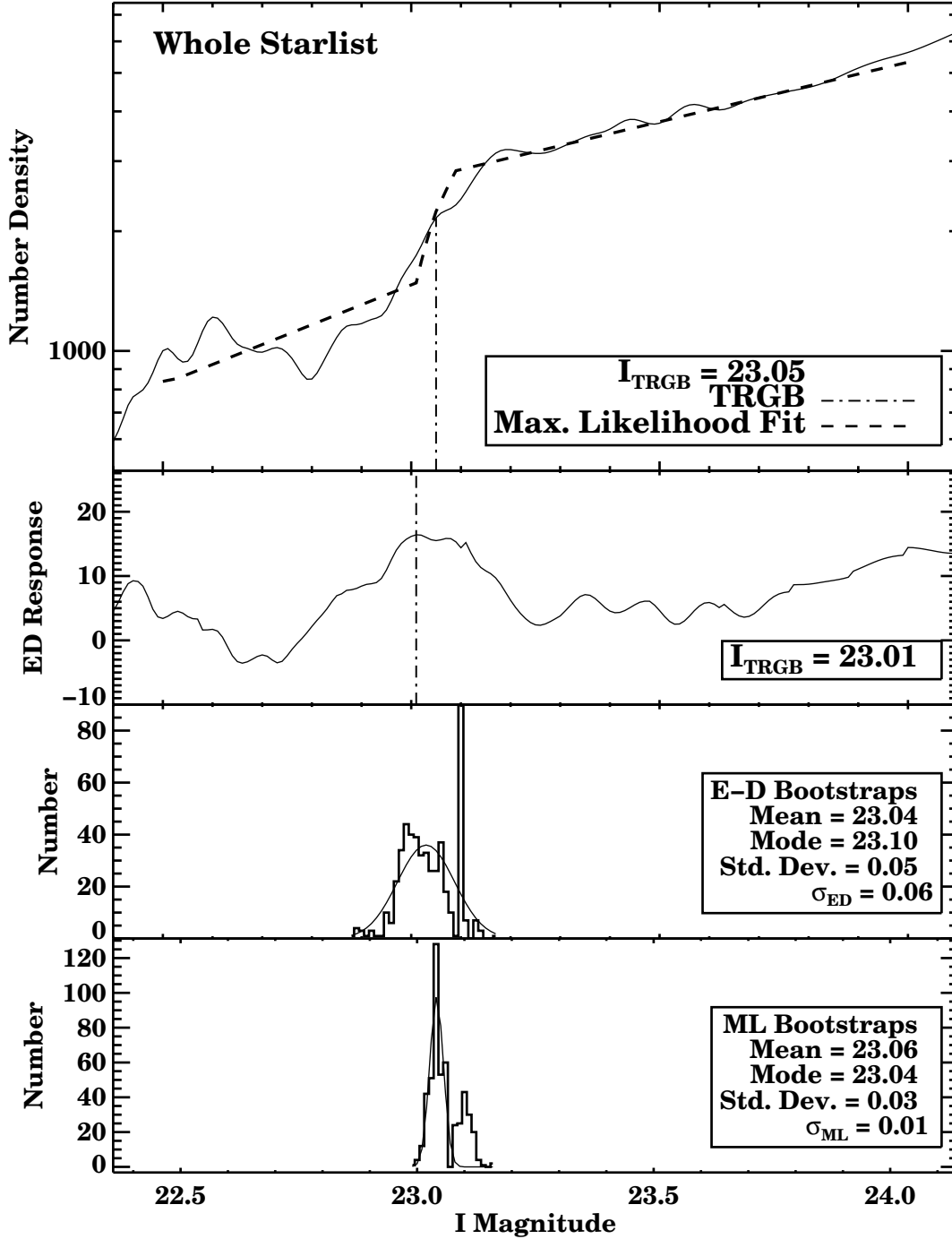
I Magnitude

Fig. 15.— Luminosity function of all stars in the *HST*/WFPC2 image of UGC 07577 (top panel). Overplotted is the best-fit model luminosity function determined via maximum likelihood analysis. The lower three panels are as in Fig. 4

Halo

Number Density

I_{TRGB} = 23.01
TRGB
Max. Likelihood Fit

ED Response

I_{TRGB} = 23.01

Number

E–D Bootstraps
Mean = 23.02
Mode = 23.00
Std. Dev. = 0.09
σ_{ED} = 0.02

Number

ML Bootstraps
Mean = 23.04
Mode = 23.02
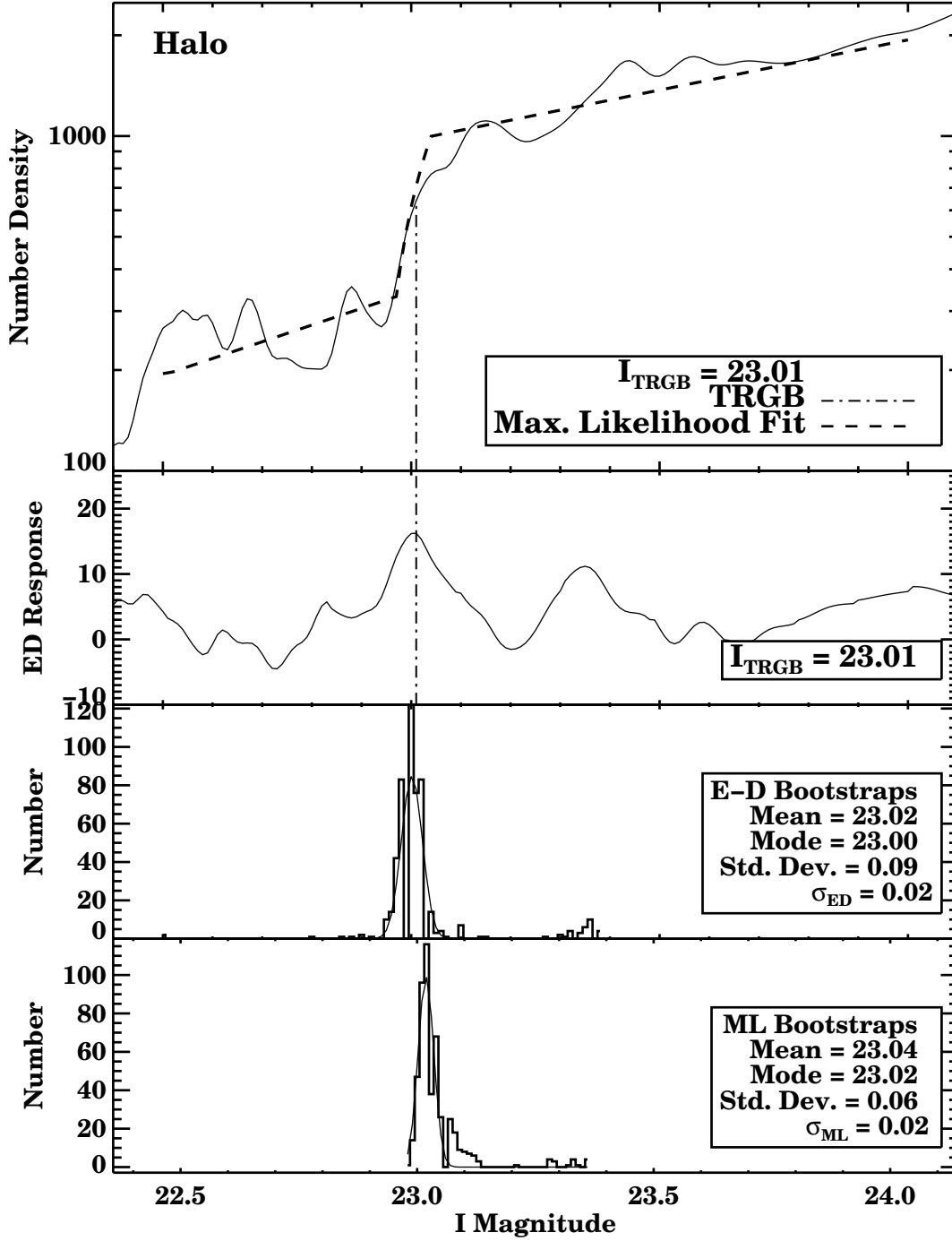Std. Dev. = 0.06
σ_{ML} = 0.02

I Magnitude

Fig. 16.— Luminosity function of stars in the halo region of UGC 07577 (top panel). Overplotted is the best-fit model luminosity function determined via maximum likelihood analysis. The lower three panels are as in Fig. 4
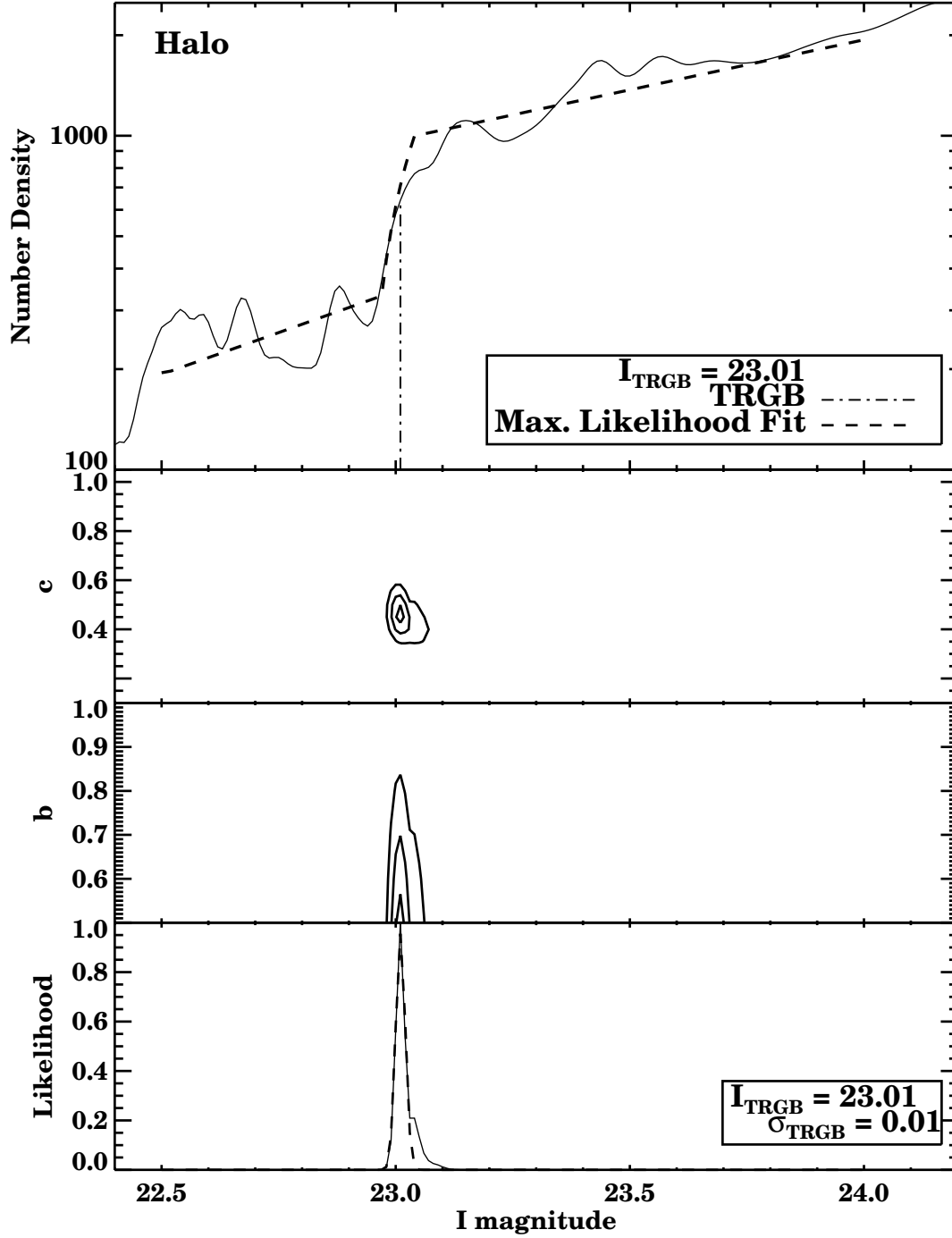
Fig. 17.— Top panel is as in Fig. 15. The second and third panels plot 1σ, 2σ, and 3σ contours of the likelihood function parameters c and b. The fourth panel plots the marginalized likelihood. A Gaussian fit with $\sigma_{\mathrm{TRGB}} = 0.01$ mag is overplotted as a dashed line.
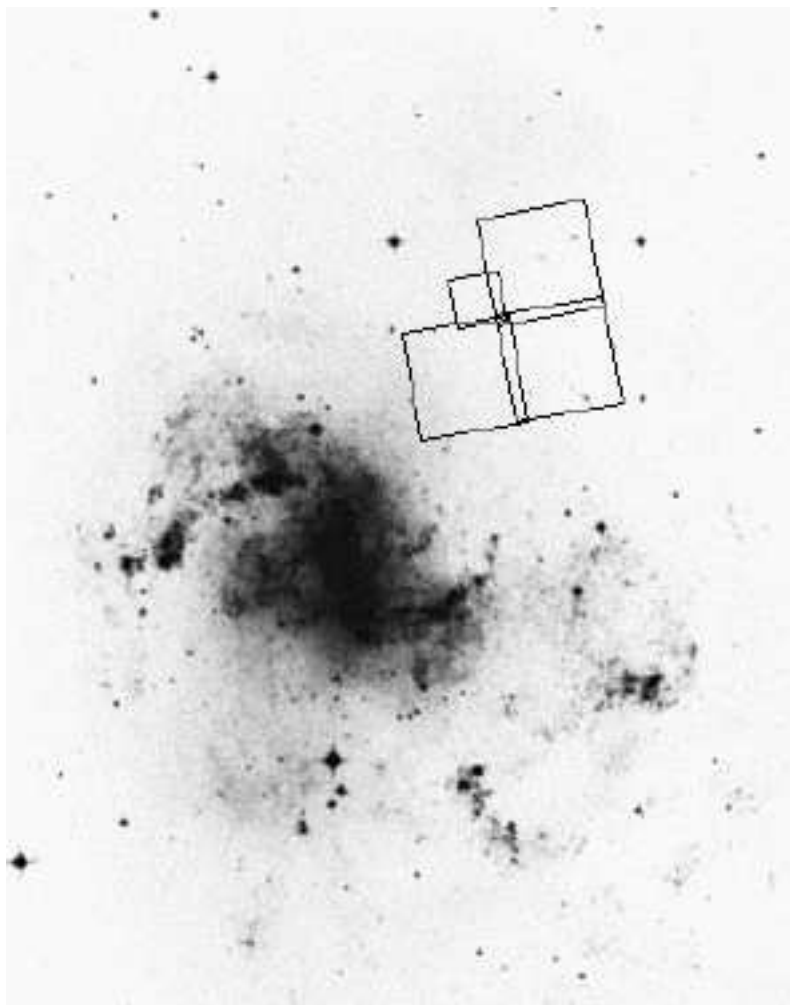
Fig. 18.— *HST*/WFPC2 footprint of our observations overlayed on a Digital Sky Survey image of NGC 1313.
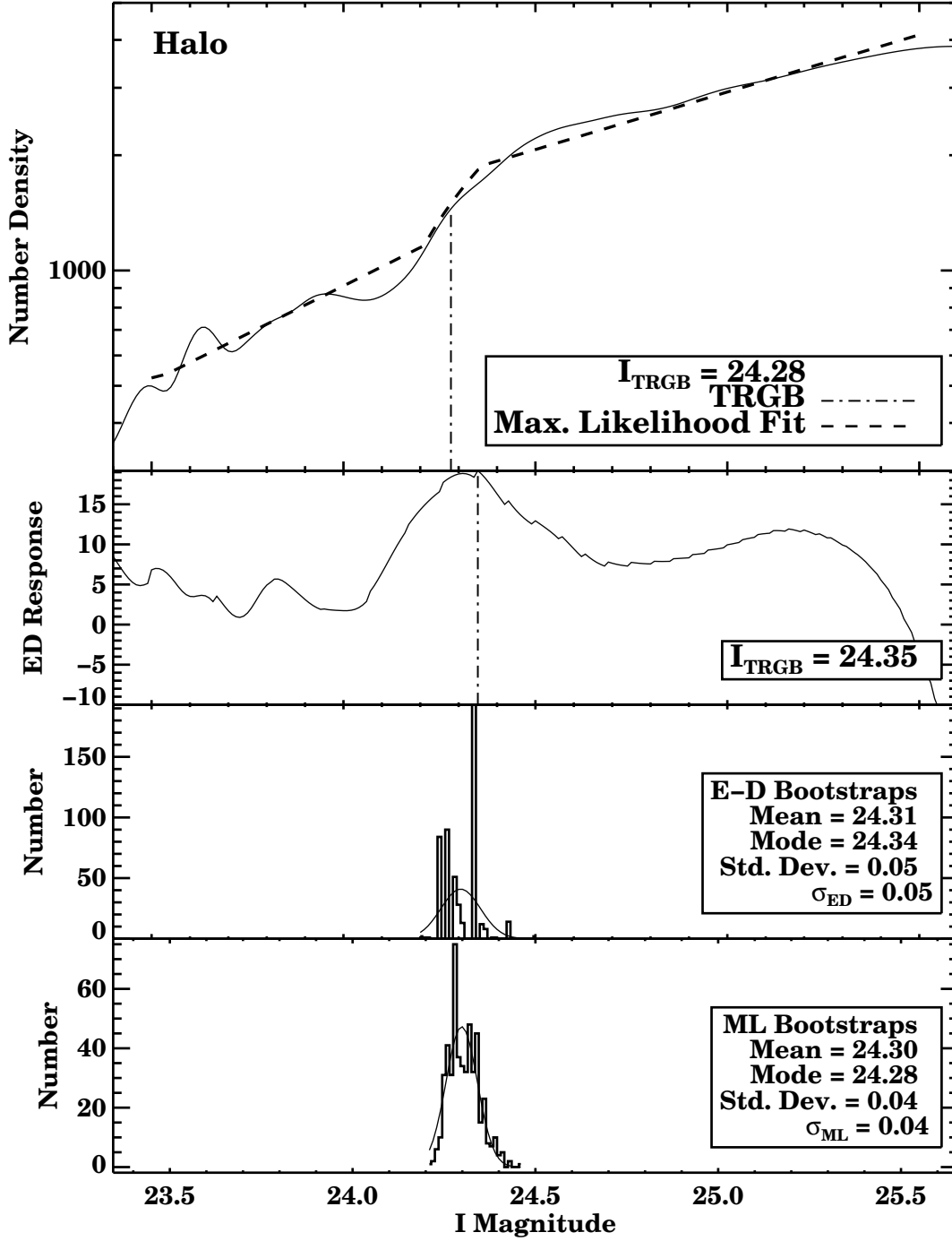
Fig. 19.— Luminosity function of stars in the halo region of NGC 1313. Overplotted is the best-fit model luminosity function determined via maximum likelihood analysis. The lower three panels are as in Fig. 4
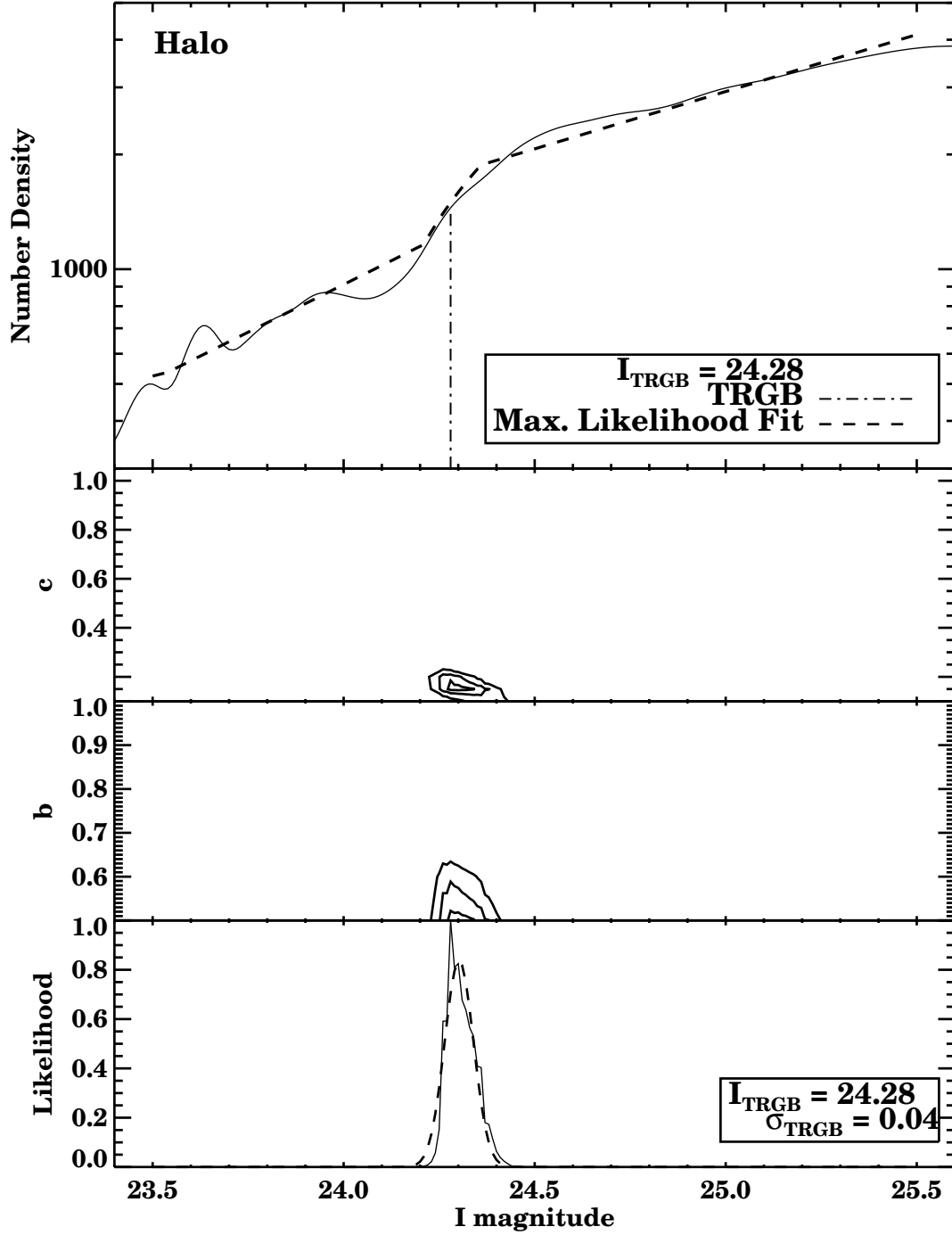
Fig. 20.— Top panel is as in Fig. 19. The second and third panels plot 1σ, 2σ, and 3σ contours of the likelihood function parameters c and b. The fourth panel plots the marginalized likelihood. A Gaussian fit with $\sigma_{\mathrm{TRGB}} = 0.04$ mag is overplotted as a dashed line.
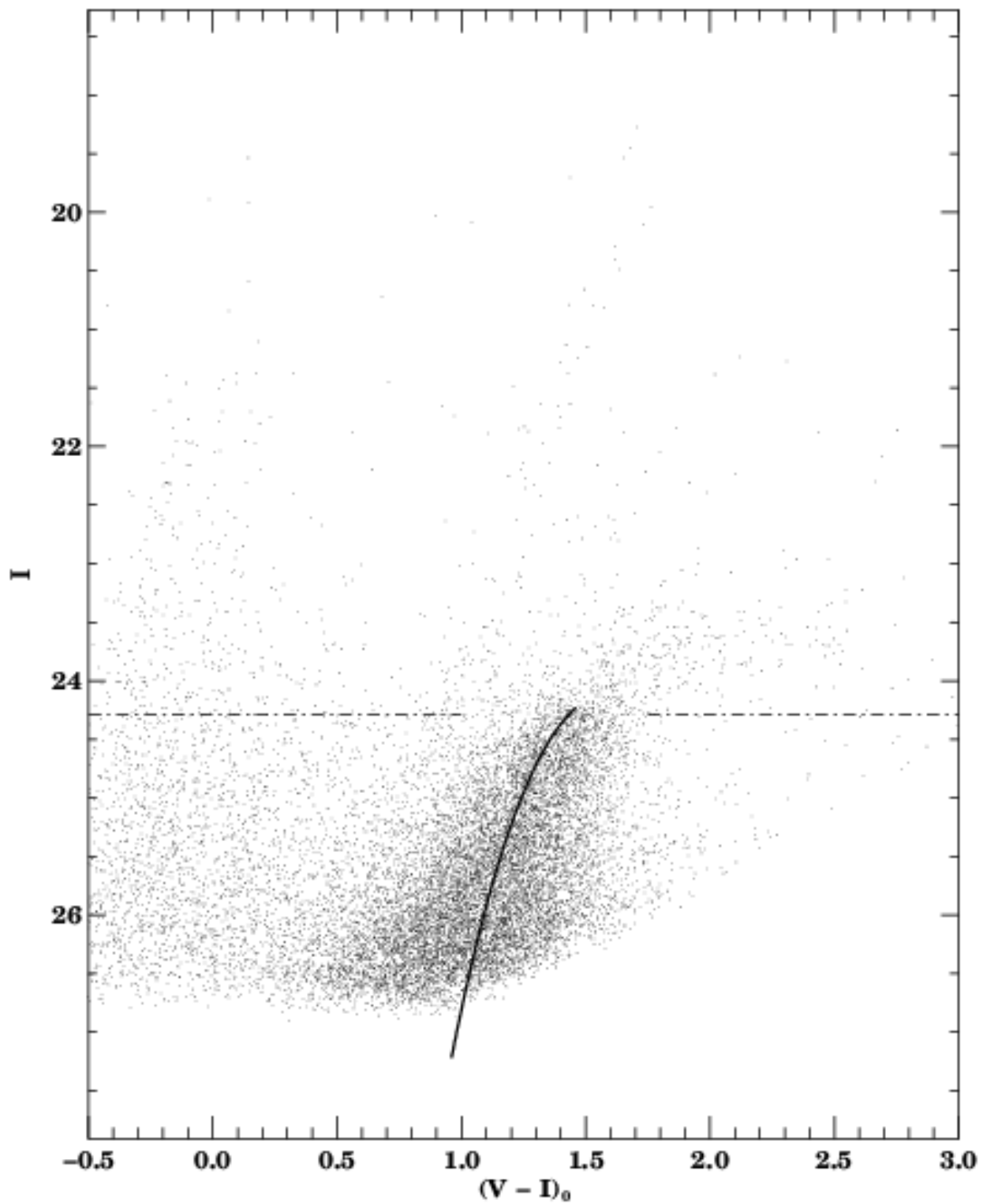
Fig. 21.— Color–Magnitude Diagram for all stars in the UGC 06456 CCD frame. The red giant branch locus (determined as discussed in the text) is also plotted.
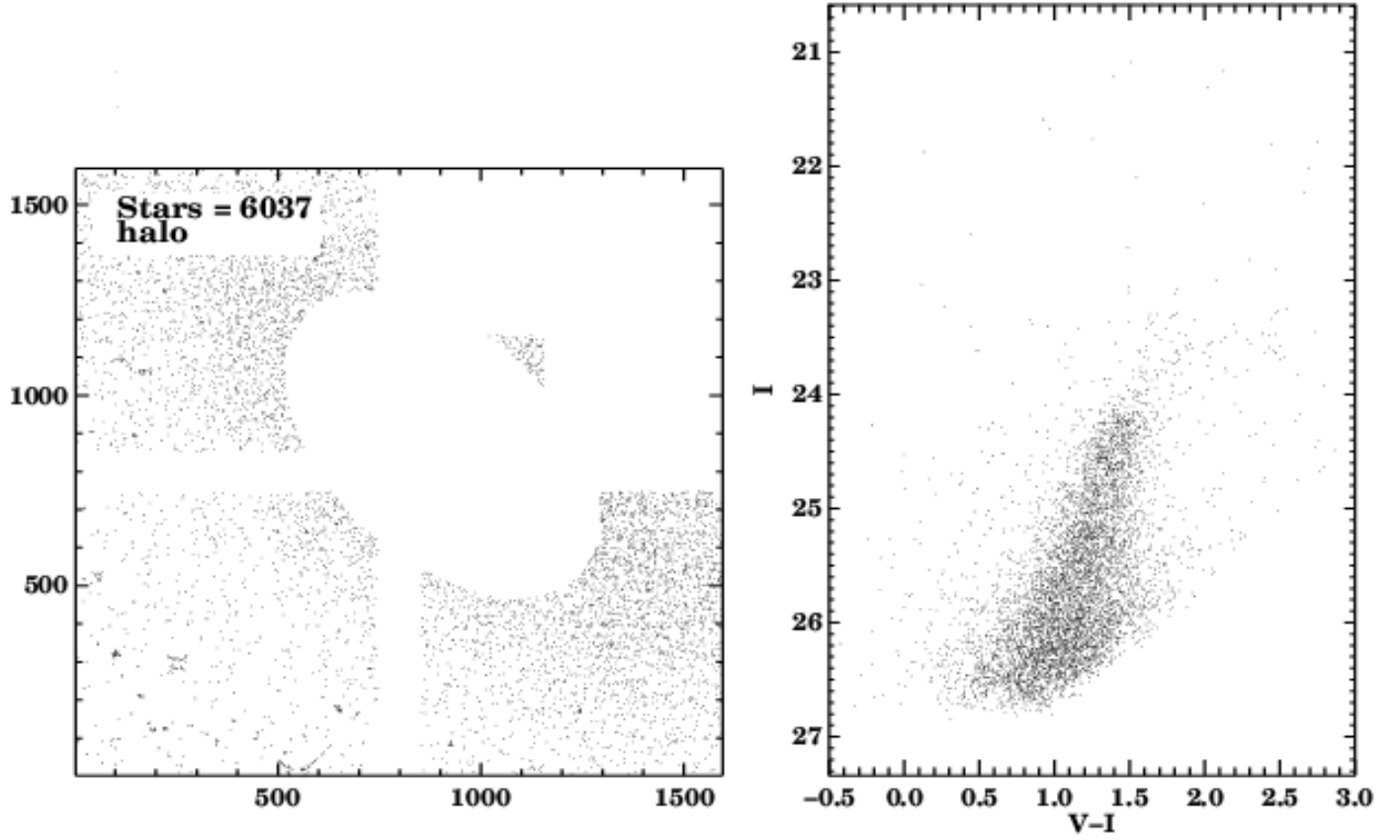
Fig. 22.— The left panel is a map of the pixel positions of all stars in the halo region of UGC 06456. The right panel is a Color–Magnitude diagram of just these stars. Notice the considerable drop in the number of blue stars from Fig. 21 after cutting out the core region.
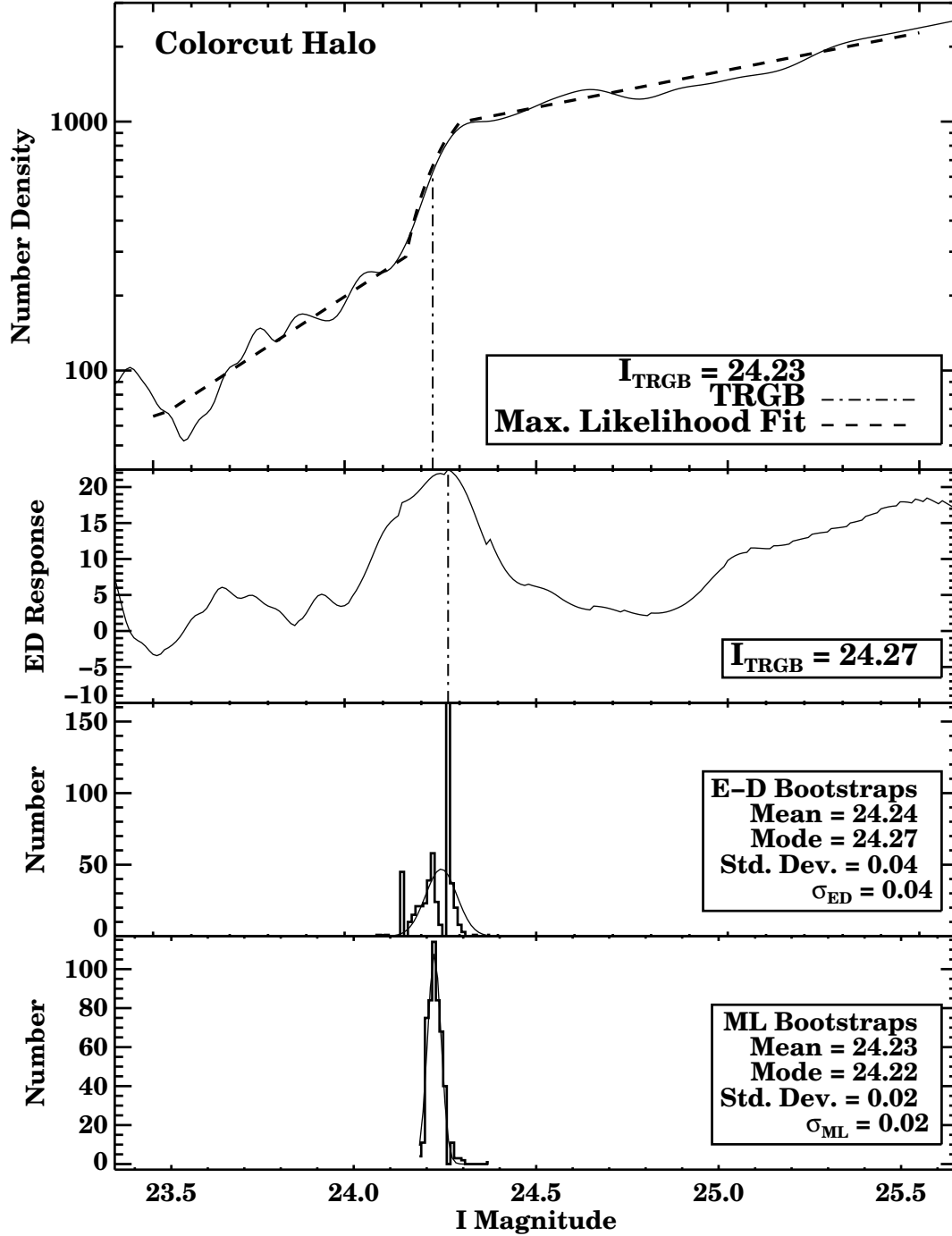
Fig. 23.— Luminosity function of stars in the halo of UGC 06456 with $0.45 \leq (V - I) \leq 1.8$ mag. Overplotted is the best-fit model luminosity function determined via maximum likelihood analysis. The lower three panels are as in Fig. 4

Fig. 24.— Top panel as in Fig 23. The second and third panels plot 1σ, 2σ, and 3σ contours of the likelihood function parameters c and b. The fourth panel plots the marginalized likelihood. A Gaussian fit with $\sigma_{\mathrm{TRGB}} = 0.02$ mag is overplotted as a dashed line.

Fig. 25.— Mosaic of a single 1300s *HST*/WFPC2 exposure of UGC 03755.
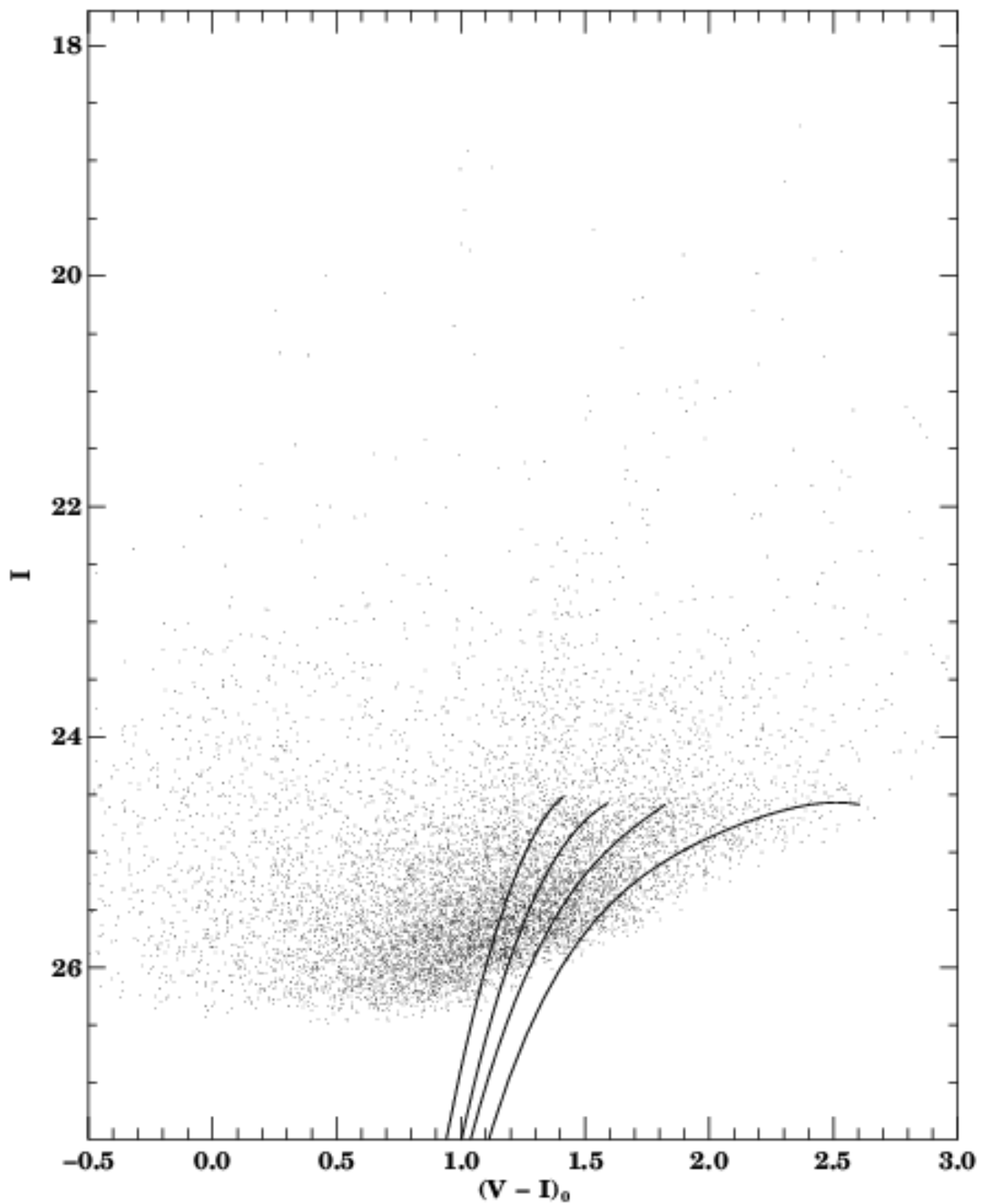
Fig. 26.— Color–Magnitude Diagram for all stars in the UGC 03755 CCD frame. The red giant branch loci of M15, M2, NGC 1851, and 47 Tuc (from left to right; see Da Costa & Armandroff 1990) are overplotted.

Fig. 27.— Luminosity function of all stars in UGC 03755. Overplotted is the best-fit model luminosity function determined via maximum likelihood analysis. The lower three panels are as in Fig. 4
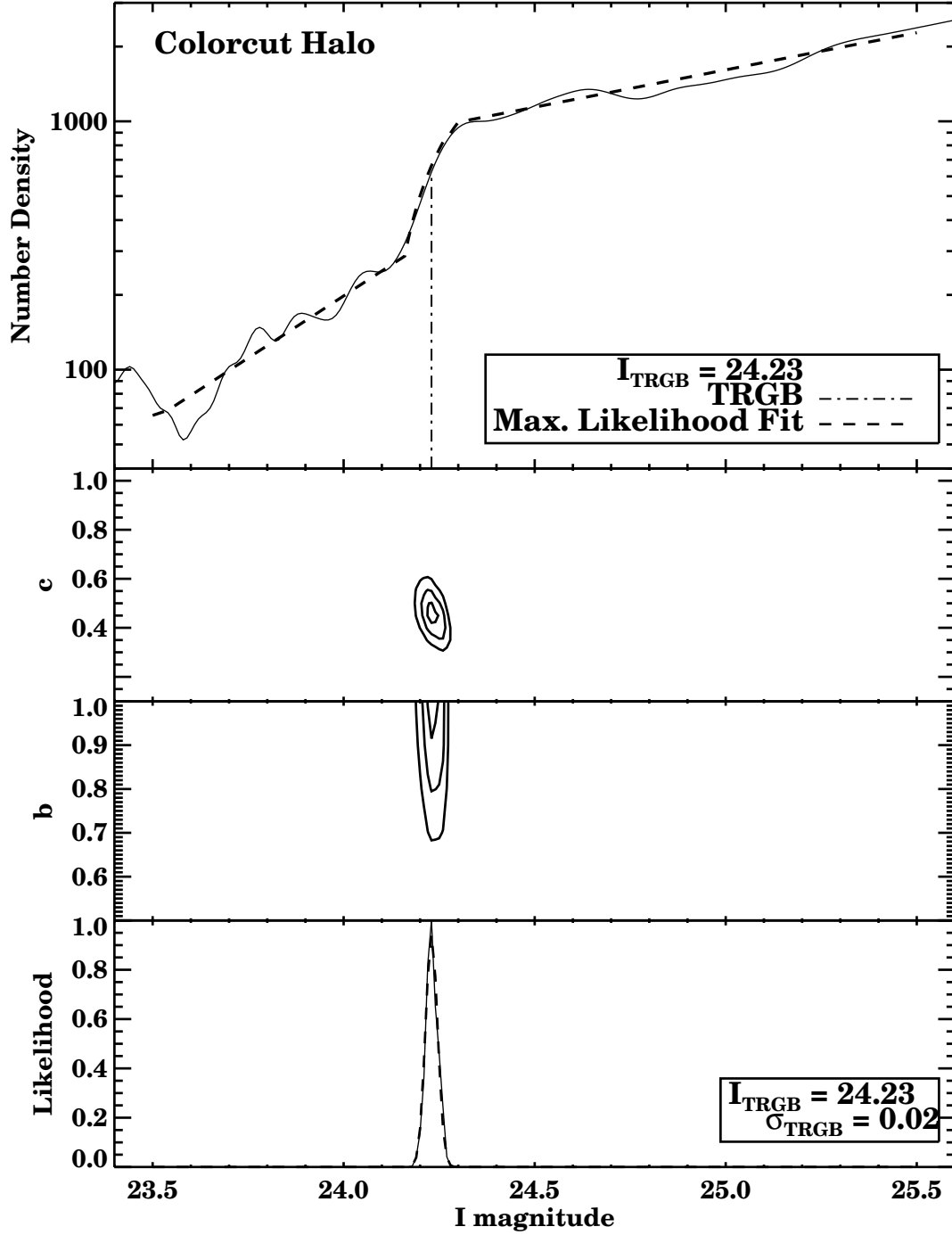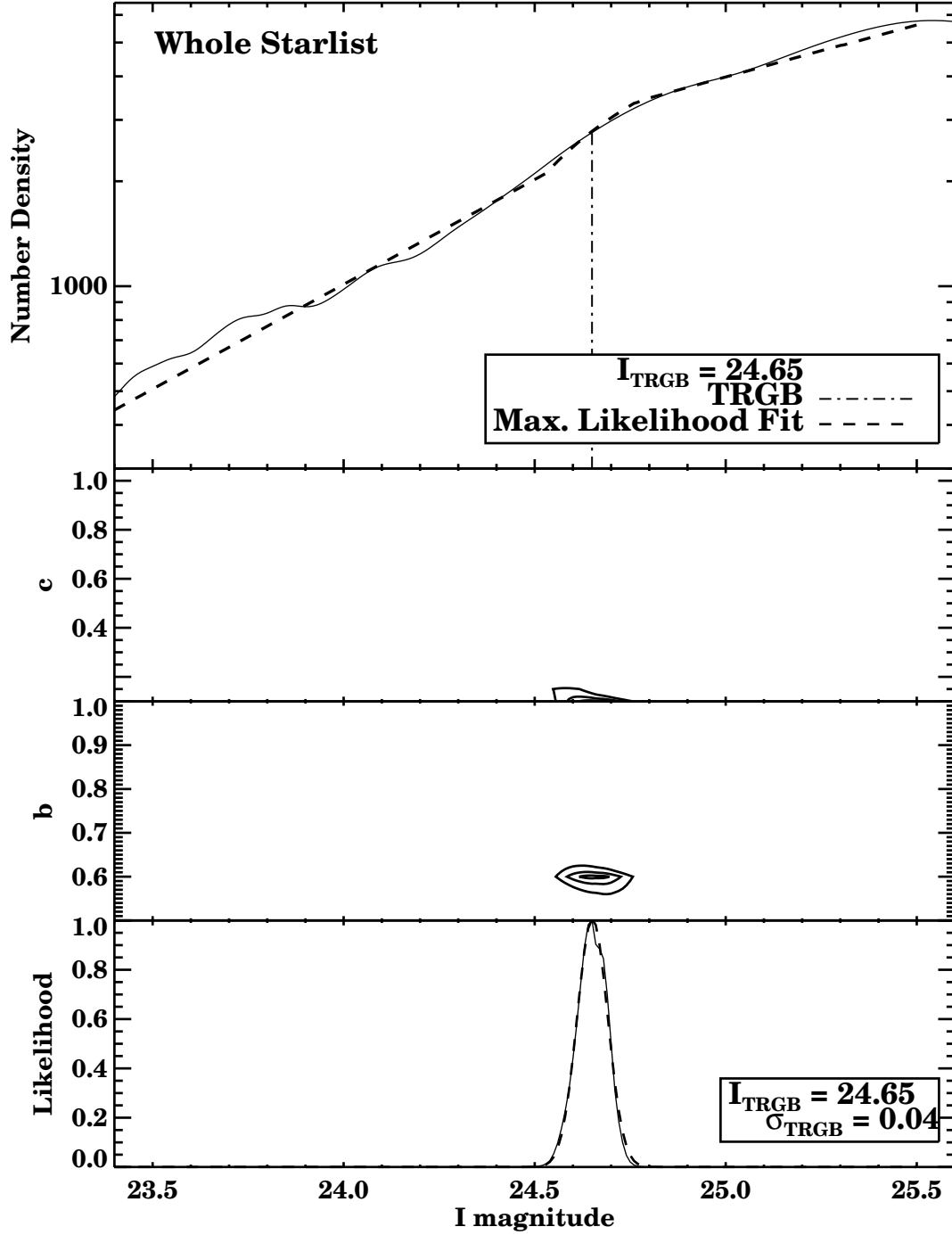
Fig. 28.— Top panel as in Fig. 27. The second and third panels plot 1σ, 2σ, and 3σ contours of the likelihood function parameters c and b. The fourth panel plots the marginalized likelihood. A Gaussian fit with $\sigma_{\mathrm{TRGB}} = 0.04$ mag is overplotted as a dashed line.
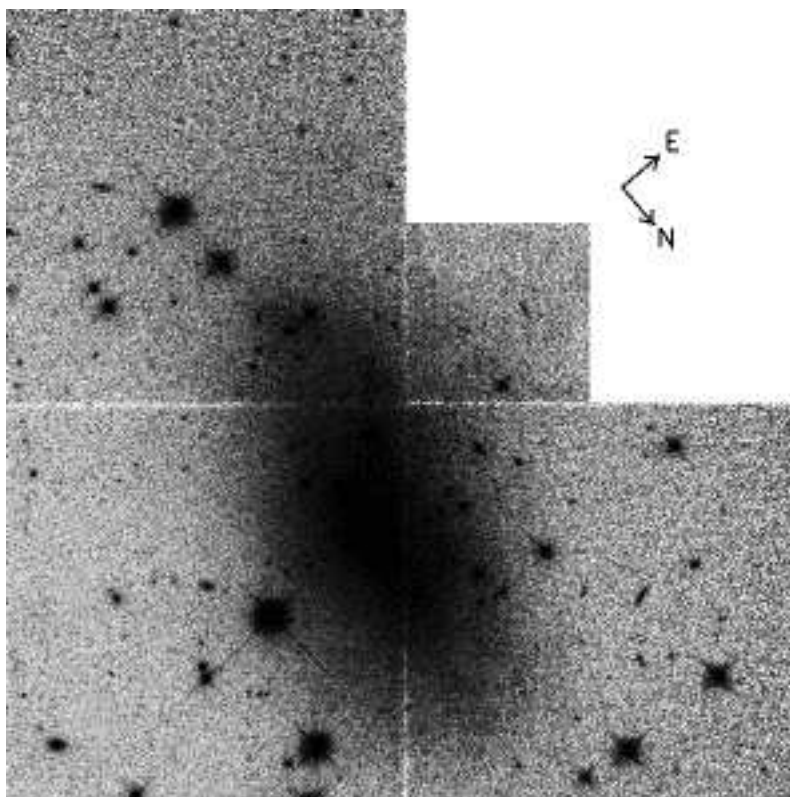
Fig. 29.— NGC 2366 Color–Magnitude Diagram for all stars in the Keck/LRIS CCD frame.
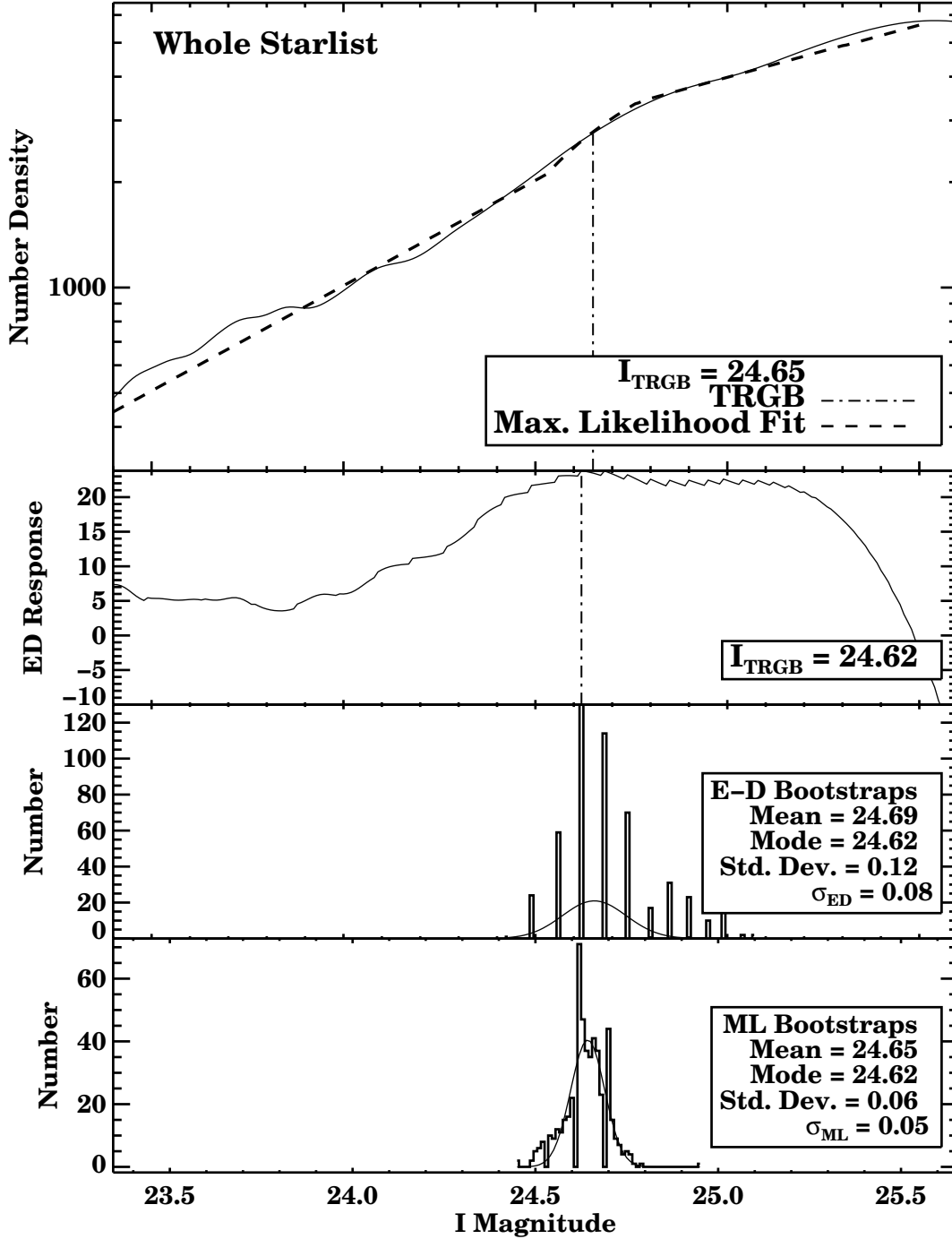
Fig. 30.— Luminosity function of all stars in NGC 2683. Overplotted is the best-fit model luminosity function determined via maximum likelihood analysis. The lower three panels are as in Fig. 4
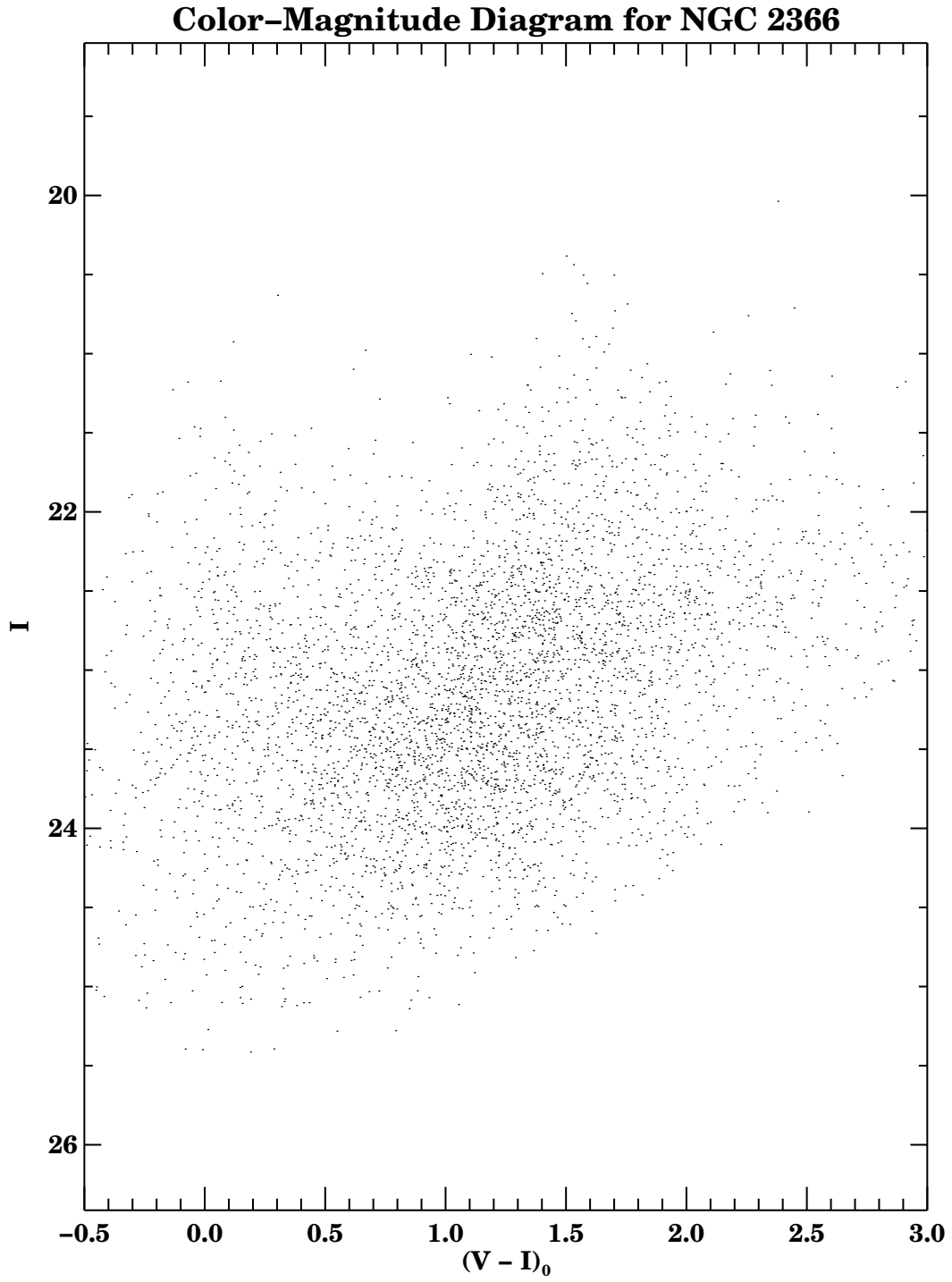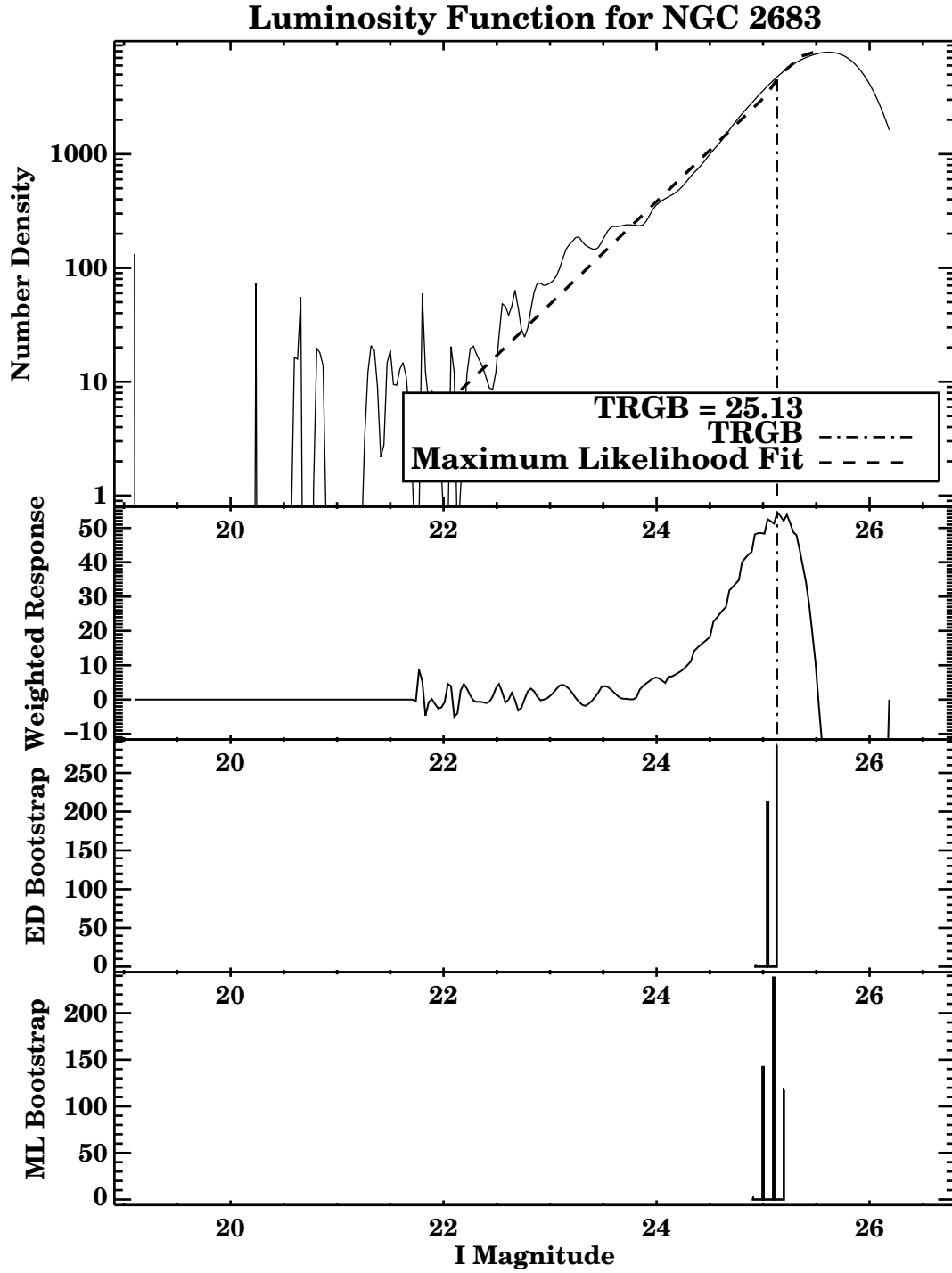
Table 1.   Details of Observations

Galaxy	l (°)	b (°)	Date (dd/mm/yy)	Instrument	Filter	# Exp.	Exp. Time/Frame (sec)	FWHM (arcsec)	Comments
Leo I	225.982	49.110	23/12/97	Keck/LRIS	I/V	2/1	300/300	0.85-0.94/0.92	Success
Sextans B	233.200	43.784	22/12/97	Keck/LRIS	I/V	1/1	300/300	0.75/0.78	Success
Holmberg I	140.729	38.662	23/12/97	Keck/LRIS	I/V	1/1	300/300	0.97/1.08	Poor Image
Holmberg II	144.283	32.691	22/12/97	Keck/LRIS	I/V	4/1	300/600	0.82-0.93/0.86	Shallow
Holmberg IX	141.977	41.052	22/12/97	Keck/LRIS	I/V	1/1	300/300	0.75/0.88	Shallow
IC 342	138.173	10.580	22/12/97	Keck/LRIS	I/V	4/1	300/600	0.77-0.90/1.02	Crowded
IC 2574	140.210	43.605	23/12/97	Keck/LRIS	I/V	3/1	250-300/300	0.91-1.02/1.02	Shallow
NGC 1560	138.367	16.022	22/12/97	Keck/LRIS	I/V	4/1	300/600	1.10-1.29/1.40	Shallow
NGC 2366	146.419	28.535	22/12/97	Keck/LRIS	I/V	4/1	300/600	0.77-1.11/0.94	Shallow
NGC 2903	208.711	44.540	22/12/97	Keck/LRIS	I/V	3/1	300/400	0.74-0.78/0.86	Shallow
NGC 2976	143.914	40.902	22/12/97	Keck/LRIS	I/V	3/1	300/400	0.87-0.94/0.84	Shallow
NGC 3109	262.101	23.070	22/12/97	Keck/LRIS	I/V	1/1	300/300	0.88/0.90	Success
UGC 02684	166.322	-32.747	22/12/97	Keck/LRIS	I/V	10/2	300-400/600-800	0.61-0.89/0.72-0.96	Unresolved
UGC 02716	166.777	-31.825	22/12/97	Keck/LRIS	I/V	7/2	300-400/600-800	$\cdots$	Unresolved
UGC 03974	203.100	18.541	22/12/97	Keck/LRIS	I/V	8/2	400-500/800-900	$\cdots$	Unresolved
UGC 04115	207.003	20.897	22/12/97	Keck/LRIS	I/V	8/2	300-400/600-800	0.64-0.83/0.76	Unresolved
UGC 05272	195.416	50.563	23/12/97	Keck/LRIS	I/V	4/1	300/600	0.77-0.80/0.78	Unresolved
UGC 05340	199.887	51.614	23/12/97	Keck/LRIS	I/V	4/1	300/600	0.74-0.92/0.94	Unresolved
IC 342	138.173	10.580	14/08/99	*HST*/WFPC2	F814W/F555W	2/2	1300/1300	$\cdots$	Crowded
IRAS 12483-1311	302.747	49.415	22/01/00	*HST*/WFPC2	F814W	2	1200	$\cdots$	Bad z
NGC 1313	283.472	-44.654	14/01/00	*HST*/WFPC2	F814W	2	1300	$\cdots$	Success
NGC 2683	190.457	38.761	15/02/00	*HST*/WFPC2	F814W	2	1300	$\cdots$	Shallow
NGC 2903	208.711	44.540	02/05/00	*HST*/WFPC2	F814W	2	1200	$\cdots$	Shallow
NGC 6503	100.574	30.640	08/11/99	*HST*/WFPC2	F814W	2	1300	$\cdots$	Shallow
UGC 03476	180.766	10.513	13/02/00	*HST*/WFPC2	F814W/F555W	2/2	1300/1300	$\cdots$	Shallow
UGC 03698	172.971	21.622	11/02/00	*HST*/WFPC2	F814W	2	1300	$\cdots$	Shallow
UGC 03755	206.013	9.715	26/03/00	*HST*/WFPC2	F814W/F555W	2/2	1200/1200	$\cdots$	Marginal
UGC 03860	177.806	23.934	02/07/00	*HST*/WFPC2	F814W	2	1300	$\cdots$	Shallow
UGC 03974	203.100	18.541	22/01/00	*HST*/WFPC2	F814W	2	1200	$\cdots$	Shallow
UGC 04115	207.003	20.897	24/09/99	*HST*/WFPC2	F814W	2	1200	$\cdots$	Shallow
UGC 07577	137.751	72.945	09/05/00	*HST*/WFPC2	F814W	2	1300	$\cdots$	Success
UGC 06456[a]	127.836	37.327	10/07/95	*HST*/WFPC2	F814W/F555W	3/3	1400/1400	$\cdots$	Success

[a]*HST*/WFPC2 archival object.

Table 2.   Distances to Nearby Galaxies

Galaxy	I_{TRGB} (mag $\pm$ r $\pm$ s)	$(V-I)_{\circ,\mathrm{TRGB}}$ (mag)	$(V-I)_{-3.5}$ (mag)	[Fe/H] (dex)	$M_{I,\mathrm{TRGB}}$ (mag $\pm$ r $\pm$ s)	A_V (mag)	A_I (mag)	$\mu_{\circ}$ (mag)	$d_{\odot}$ (Mpc)
				Using Maximum Likelihood Method					
Leo I	$18.14 \pm 0.07 \pm 0.05$	1.39 ± 0.02	1.28 ± 0.02	-1.94 ± 0.08	$-3.98 \pm 0.02 \pm 0.04$	0.12 ± 0.01	0.07 ± 0.01	22.05 ± 0.10	0.26 ± 0.01
NGC 3109	$21.63 \pm 0.05 \pm 0.03$	1.46 ± 0.02	1.34 ± 0.02	-1.69 ± 0.06	$-4.02 \pm 0.01 \pm 0.02$	0.22 ± 0.02	0.13 ± 0.01	25.52 ± 0.06	1.27 ± 0.04
Sextans B	$21.68 \pm 0.02 \pm 0.02$	1.44 ± 0.01	1.33 ± 0.01	-1.73 ± 0.04	$-4.01 \pm 0.01 \pm 0.02$	0.10 ± 0.01	0.06 ± 0.01	25.63 ± 0.04	1.34 ± 0.02
UGC 07577	$23.01 \pm 0.06 \pm 0.02$	$\cdots$	$\cdots$	$\cdots$	-4.01 ± 0.03	0.07 ± 0.01	0.04 ± 0.00	26.98 ± 0.07	2.49 ± 0.08
NGC 1313	$24.28 \pm 0.04 \pm 0.02$	$\cdots$	$\cdots$	$\cdots$	-4.01 ± 0.03	0.36 ± 0.04	0.21 ± 0.02	28.08 ± 0.06	4.13 ± 0.11
UGC 06456	$24.23 \pm 0.02 \pm 0.02$	1.46 ± 0.02	1.36 ± 0.01	-1.62 ± 0.05	$-4.03 \pm 0.01 \pm 0.01$	0.12 ± 0.01	0.07 ± 0.01	28.19 ± 0.04	4.34 ± 0.07
UGC 03755	$24.65 \pm 0.06 \pm 0.02$	$\cdots$	$\cdots$	$\cdots$	-4.01 ± 0.03	0.29 ± 0.03	0.17 ± 0.02	28.49 ± 0.07	4.98 ± 0.17
				Using Edge-Detection Method					
Leo I	$18.14 \pm 0.11 \pm 0.05$	1.39 ± 0.02	1.28 ± 0.02	-1.93 ± 0.07	$-3.99 \pm 0.01 \pm 0.04$	0.12 ± 0.01	0.07 ± 0.01	22.06 ± 0.13	0.26 ± 0.02
NGC 3109	$21.60 \pm 0.08 \pm 0.03$	1.46 ± 0.02	1.35 ± 0.02	-1.66 ± 0.06	$-4.02 \pm 0.01 \pm 0.02$	0.22 ± 0.02	0.13 ± 0.01	25.49 ± 0.09	1.25 ± 0.05
Sextans B	$21.68 \pm 0.05 \pm 0.02$	1.44 ± 0.01	1.33 ± 0.01	-1.73 ± 0.03	$-4.01 \pm 0.01 \pm 0.02$	0.10 ± 0.01	0.06 ± 0.01	25.63 ± 0.06	1.34 ± 0.04
UGC 07577	$23.01 \pm 0.09 \pm 0.02$	$\cdots$	$\cdots$	$\cdots$	-4.01 ± 0.03	0.07 ± 0.01	0.04 ± 0.00	26.98 ± 0.10	2.49 ± 0.11
NGC 1313	$24.35 \pm 0.05 \pm 0.02$	$\cdots$	$\cdots$	$\cdots$	-4.01 ± 0.03	0.36 ± 0.04	0.21 ± 0.02	28.15 ± 0.07	4.26 ± 0.13
UGC 06456	$24.27 \pm 0.04 \pm 0.02$	1.45 ± 0.01	1.35 ± 0.01	-1.64 ± 0.05	$-4.03 \pm 0.01 \pm 0.01$	0.12 ± 0.01	0.07 ± 0.01	28.23 ± 0.05	4.42 ± 0.10
UGC 03755	$24.62 \pm 0.12 \pm 0.02$	$\cdots$	$\cdots$	$\cdots$	-4.01 ± 0.03	0.29 ± 0.03	0.17 ± 0.02	28.46 ± 0.13	4.92 ± 0.29
				Estimates made by other authors					
NGC 2366	≤ 23.74	$\cdots$	$\cdots$	$\cdots$	-4.01	0.12 ± 0.01	0.07 ± 0.01	$\leq 27.68 \pm 0.20$	$\leq 3.44 \pm 0.32$
UGC 03755	24.24	$\cdots$	$\cdots$	$\cdots$	-4.01	0.29 ± 0.03	0.17 ± 0.02	28.08 ± 0.39	4.13 ± 0.74
NGC 2683	25.49	$\cdots$	$\cdots$	$\cdots$	-4.01	0.11 ± 0.01	0.06 ± 0.01	29.44 ± 0.36	7.73 ± 1.28
				Lower limits inferred from photometry					
NGC 2366	≥ 23.00	$\cdots$	$\cdots$	$\cdots$	-4.01	0.12 ± 0.01	0.07 ± 0.01	≥ 26.94	≥ 2.44
UGC 03755	≥ 24.50	$\cdots$	$\cdots$	$\cdots$	-4.01	0.29 ± 0.03	0.17 ± 0.02	≥ 28.34	≥ 4.65
NGC 2683	≥ 25.00	$\cdots$	$\cdots$	$\cdots$	-4.01	0.11 ± 0.01	0.06 ± 0.01	≥ 28.95	≥ 6.15